Supplementary Information for Adloff et al. 2024

Ocean circulation changes

The ocean circulation changes in all experiments due to the prescribed changes in insolation, radiative forcings from greenhouse gasses and land albedo. These forcings result in cyclic transitions between interglacial and glacial circulation states. The glacial states show a reduction of the Atlantic Meridional Overturning Circulation (AMOC) by up to 4.5 Sv and an increase of the shallow overturning cell in the equatorial Pacific north of the Equator of up to 1 Sv compared to the PI (Fig S9). Accordingly, water mass ages increase below 2000 m in the North Atlantic and decrease in the South Atlantic and Pacific during glacials. With additional wind stress reductions in the Southern Ocean (SO, $<40°$S, simulation SOWI), the South Pacific downwelling is strengthened by up to 1.5 Sv locally in glacials, and the AMOC strength further reduced by up to 1 Sv. The increased stratification in the SO reduces upwelling and increases the water mass age throughout the Pacific and South Atlantic by up to 150 years. The slower AMOC also results in $\sim$100 yr older waters below 2000 m in the North Atlantic. If instead of the wind stress the glacial radiative forcing is further reduced (by 2.5 Wm^{-2}, simulation AERO), AMOC weakens in all glacials by up to 12 Sv relative to PI during the glacial maxima (the model behaviour to this forcing is described more extensively in Adloff et al., 2023). The Pacific circulation is much less affected, showing only a small decrease (up to 1 Sv) in the Pacific Meridional Overturning Circulation (PMOC, here evaluated at $30\mathrm{deg}$S). As a result of the AMOC collapse, the Atlantic water mass age increase caused by the standard forcing is amplified, with an aging of up to 1000 years in the deep North Atlantic as glacial deep water formation now only occurs in the Southern Ocean.

These circulation changes are largest in MIS 16a, 6a and 2, when the respective forcings are strongest, and also appear in interglacials that were colder than the PI, although at much smaller amplitude.

Effects of orbital, insolation and albedo changes on carbon fluxes

In the following, we examine the underlying glacial-interglacial carbon cycle changes and the effect of interactive sediments under each forcing. First we focus on the standard forcing, before discussing the effects of additional forcings.

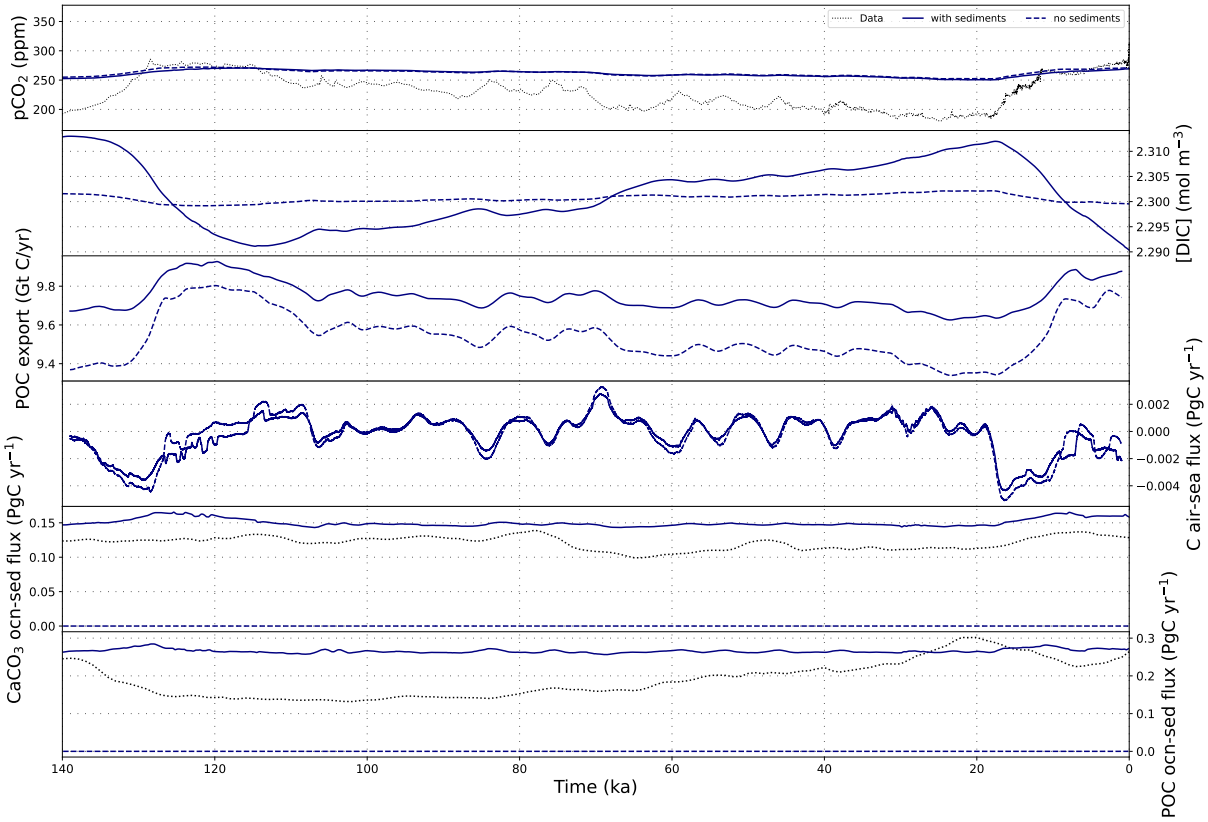

Figure S1. Atmospheric CO_2 concentrations, DIC and carbon fluxes over the most recent full glacial cyle in simulation BASE with and without dynamic sediments.

The dynamic circulation and climate affect the partitioning of carbon between the interactive carbon reservoirs in the model (atmosphere, ocean, reactive sediments and lithosphere). The applied forcings vary the CO_2 concentration gradient between air and seawater by modifying CO_2 solubility and surface ocean DIC and alkalinity concentrations. Without dynamic sediments (Fig S1), carbon in response moves between the atmosphere, the marine DIC and, to a lesser extent, DOC reservoirs in the ocean. With the standard forcing, CO_2 and O_2 solubilities increase during glacial phases because of the cooling surface ocean, leading to a steady marine uptake of carbon and oxygen from the atmosphere from peak interglacial through to the glacial maximum. The cooling reduces deep water formation rates in the North Atlantic and increases deep water formation in the Southern Ocean. These circulation changes increase the marine uptake of CO_2 while expanding sea ice prevents outgassing of marine CO_2 in the Southern Ocean. Circulation changes also redistribute dissolved nutrients. Polar export production declines due to the amplified cooling in polar oceans and expanding sea ice, causing an overall productivity decrease during glaciation despite increased primary productivity in mid-latitudes and sub-tropics due to the circulation-driven reduction of nutrient transport into the polar oceans. In the high latitudes, POC and $CaCO_3$ export fluxes decrease, predominantly due to sea ice growth, in places also because of reduced nutrient supply and lower temperatures. These export fluxes changes, particularly in

the Southern Ocean, alter phosphate cycling: In interglacial states, high export fluxes effectively transfer phosphate from the photic zone to the intermediate ocean, where most exported POC is remineralized. Upwelling of intermediate water masses returns phosphate to the surface ocean. In glacial states, less of the phosphate upwelling in the Southern Ocean is incorporated into POC and exported to intermediate ocean depths. Instead, it is downwelled and incorporated into bottom waters. In consequence, the glacial deep ocean is enriched in preformed phosphate, while phosphate concentrations at intermediate depth decrease due to climate-driven export reduction. In the surface, reduced upwelling of nutrients and reduced nutrient uptake result in almost no net change of nutrient concentrations. During deglaciation, surface and deep waters warm and upwelling as well as export fluxes are restored. Hence, decreases in atmospheric CO_2 concentration during the onsets of glaciations are directly mirrored by increases in marine DIC and decreases in marine DOC, and the inverse occurs during deglaciation.

When interactive sediments are included in the simulations, export production and ocean chemistry changes also alter sediment burial and dissolution fluxes, resulting in more than 10x larger DIC fluctuations over a glacial cycle than in the previous, closed system. Changes in net sea-air gas exchange across the glacial cycle ($\sim$0.007 PgC/yr) are smaller than changes in each POC and $CaCO_3$ burial rates ($\sim$0.02 PgC/yr). $CaCO_3$ burial is predominantly driven by productivity changes and peaks during interglacials. In glacials, $CaCO_3$ burial is reduced below areas with reduced euphotic zone $CaCO_3$ export, e.g. in the high latitudes, but additionally where $CaCO_3$ becomes unstable due lower temperatures or reduced pH due to increased sedimentary POC oxydation rates. The standard forcing is not sufficient to cause wide-spread O_2 depletion in the glacial deep ocean, hence under the standard forcing POC burial rates are driven by export production rates, with less/more burial in areas with reduced/increased POC export production, respectively. The exception is the upwelling zone in the Equatorial East Pacific and parts of the Indian Ocean, where increased POC export depletes benthic and sediment pore water O_2 during glacial phases. During deglaciations, sea ice recedes, ocean ventilation increases and the surface and intermediate oceans warm, fostering increased primary productivity. While productivity and POC burial increase quickly in the subpolar regions, POC burial rates in the Eastern Equatorial Pacific respond more slowly to the warming: Long turnover timescales of pore water O_2 in sediments and remineralisation of previously deposited POC delay the return of interglacial POC remineralisation rates relative to export rates from the surface ocean. Therefore, deglaciations are marked by faster productivity increases in the surface ocean than sedimentary POC remineralisation. This results in a 'sweet spot' during glacial terminations, when tropical POC burial is still higher than in the interglacial while extratropical POC export and burial has already recovered to interglacial levels, particularly during the last 400 kyr which show larger glacial-interglacial temperature contrasts and faster warming rates during deglaciations. This 'sweet spot' causes the maximum of global POC burial to occur during deglaciation, before the full interglacial.

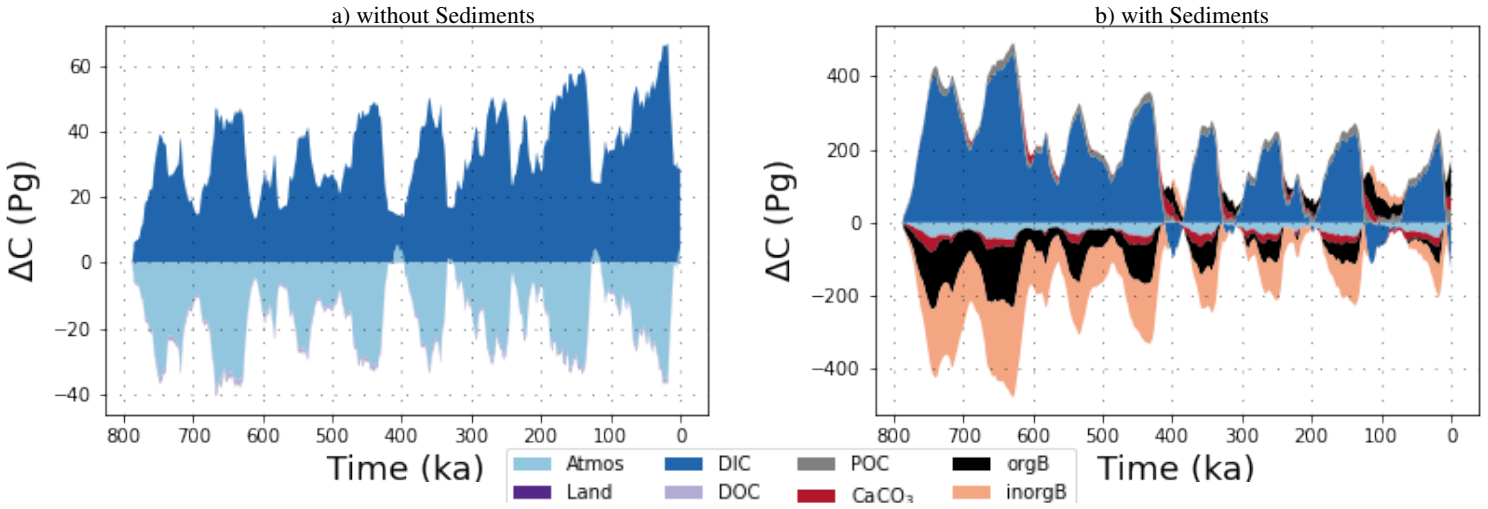

Figure S2. Transient carbon reservoir size changes across the last 780kyr as simulated in simulations with the standard (orbital, radiation and albedo) forcings in simulation BASE with and without dynamic marine sediments. Shown are the size changes of atmospheric, terrestrial, marine (DIC and DOC), sedimentary (POC and $CaCO_3$) and lithospheric (organic and inorganic) carbon storage. Note that the y-axis scale is an order of magnitude larger in b) than in a).

Introducing sediments (and a constant weathering flux) also changes carbon cycle dynamics over multiple glacial cycles. Fig S2 shows the transient changes in the simulated carbon reservoirs in simulation BASE over the entire simulated time period. In our set-up, carbon exchange between the atmosphere, ocean and sediments reacts to climatic and biochemical changes while weathering input fluxes of DIC, alkalinity and PO_4^{3-} are constant over time. A carbon flux imbalance arises during glacial phases in this open system. Under purely physical forcings, export fluxes from the photic zone decrease during glacial phases. Despite locally increased sedimentary POC preservation, global sediment accumulation rates decrease. In consequence, transfer of $CaCO_3$ and POC from the reactive sediments to the lithosphere (i.e. sediment burial) is reduced as well, since it is governed by the mass accumulation rate. The carbon which would have otherwise been buried instead accumulates as DIC in the ocean. Acceleration of sediment mass accumulation rates during glacial terminations increases the carbon transfer into the lithosphere, which reduces marine DIC. The strength of these carbon cycle responses depends on the forcing strength, which varies between glacial cycles. The lukewarm interglacials of the first 350 kyr of our simulations do not restore the export fluxes and sedimentary $CaCO_3$ preservation required to re-balance the geologic carbon cycle, and so marine DIC concentrations are persistently higher during 800-450ka than at PI. Interglacials of the last 450kyr of the simulation reduce DIC in the long-term because they are warm and long enough for increased carbon transfer into sediments and the lithosphere.

Effects of additional forcings and Earth system changes on carbon fluxes

The previously described carbon cycle changes vary when further forcings and Earth system changes are applied.

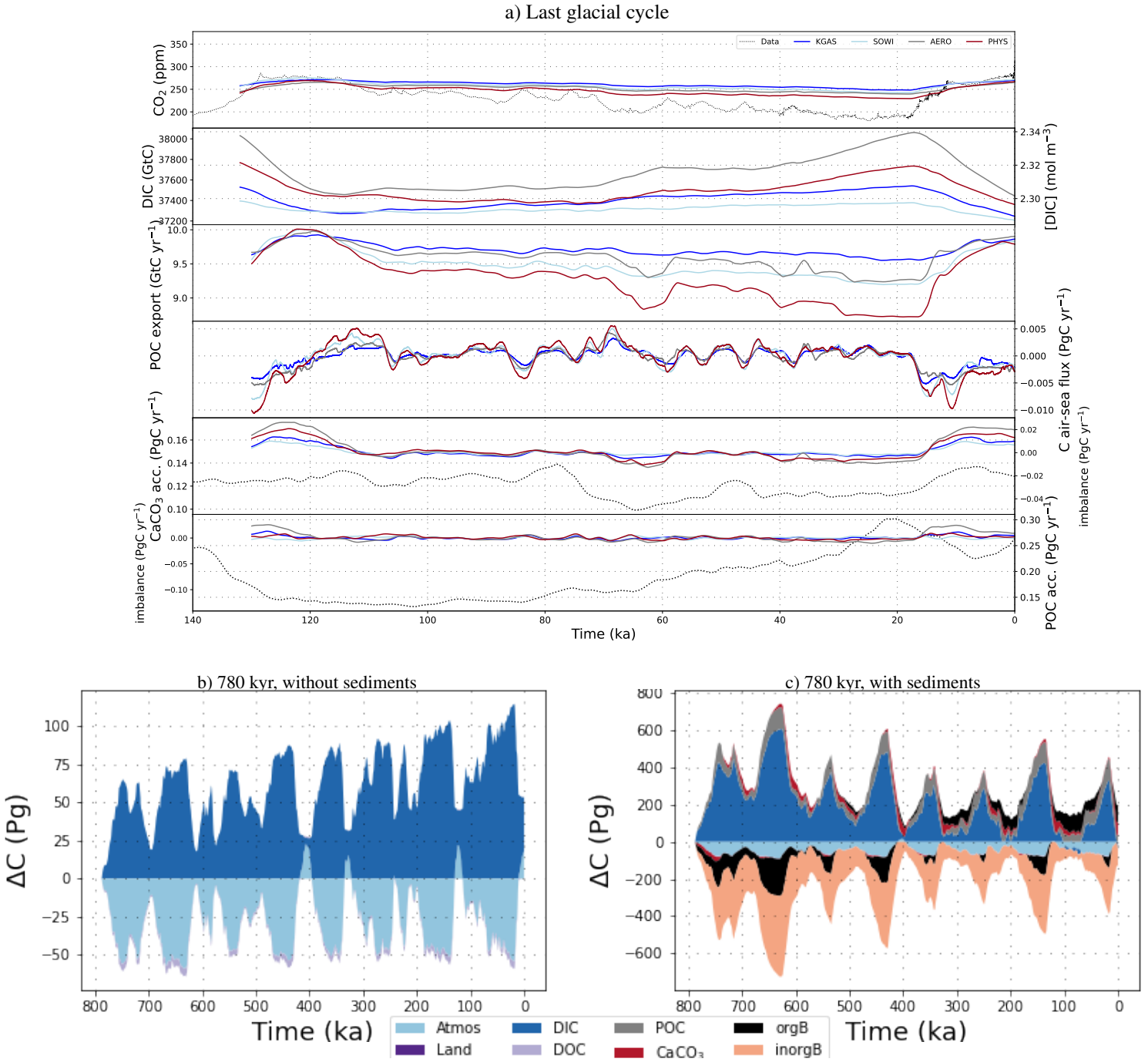

Figure S3. a) Atmospheric CO_2 concentrations, DIC and carbon fluxes over the most recent full glacial cyle in simulations with additional physical forcings in an open system. b) Transient carbon reservoir size changes across the last 780 kyr as simulated with all additional physical forcings combined in a closed system and c) in an open system. Shown are the size changes of atmospheric, terrestrial, marine (DIC and DOC), sedimentary (POC and $CaCO_3$) and lithospheric (organic and inorganic) carbon storage. Reservoir changes for individual forcings are displayed in Fig S10. Flux timeseries for simulations in a closed system are displayed in Fig S11.

Additional physical forcings result in roughly 1.5x larger carbon fluxes (Fig. S3), partially by amplifying the processes under the standard forcing and partially by introducing additional ones. Additional reduction of wind stress in the Southern Ocean (simulation SOWI) leads to a stronger isolation of deep Pacific water masses, reducing benthic oxygen levels and pH and increasing the carbon content of the glacial deep Pacific. With dynamic sediments, more organic matter and $CaCO_3$ reaching the sediments is preserved due to the reduced oxygen concentrations, particularly in Pacific upwelling zones. This results in a larger net removal of nutrients and carbon from the ocean during glacial times which would have otherwise been released at intermediate depth. In consequence, wind stress forcing over the Southern Ocean reduces the carbon content of Pacific deep water when dynamic sediments are considered, despite an increase in water mass age. The re-ventilation of the deep Pacific during glacial termination leads to rising benthic oxygen concentrations. Due to the lower storage of dissolved nutrients and carbon in the glacial deep ocean, the potential to upwell nutrients during deglaciation is reduced, suppressing the spike in POC burial during terminations seen under the standard forcing and reducing PIC burial during these transition phases.

Reducing the transfer velocity of CO_2 in the Southern Ocean during glacials (simulation KGAS) also reduces CO_2 outgassing in the Southern Ocean which increases DIC in the deep Pacific but leaves ocean circulation unaffected, which reduces its global impact and, unlike the wind forcing, does not trap nutrients in the deep Pacific.

The AMOC slow-down in simulations with an additional reduction of incoming radiation during glacial phases and especially glacial maxima (e.g. via aerosol dimming, simulation AERO) creates an old, nutrient-rich and O_2-poor bottom water mass in the glacial Atlantic. Unlike with a vigorous AMOC, nutrients are not returned as quickly to the surface Atlantic but accumulate in the deep. The additional cooling combined with reduced nutrient supply reduces POC and $CaCO_3$ export in the Atlantic. In the North, where sea ice extent is increased and temperatures drop the most, they cease entirely. Globally, the additional cooling increases CO_2 and O_2 solubility. Overall these effects increase glacial carbon storage in the deep ocean. With dynamic sediments, the reduced $CaCO_3$ export in the North Atlantic raises the local lysocline, causing dissolution and increased marine DIC concentrations. The sudden shift in water masses when AMOC resumes during deglaciation amplifies the spike in burial rates observed under the standard forcing.

The different carbon and nutrient fluxes under these forcings change the total carbon and nutrient inventories in simulations with an open system, resulting in different DIC and nutrient concentrations at the start of the last glacial cycle and at the end of the runs.

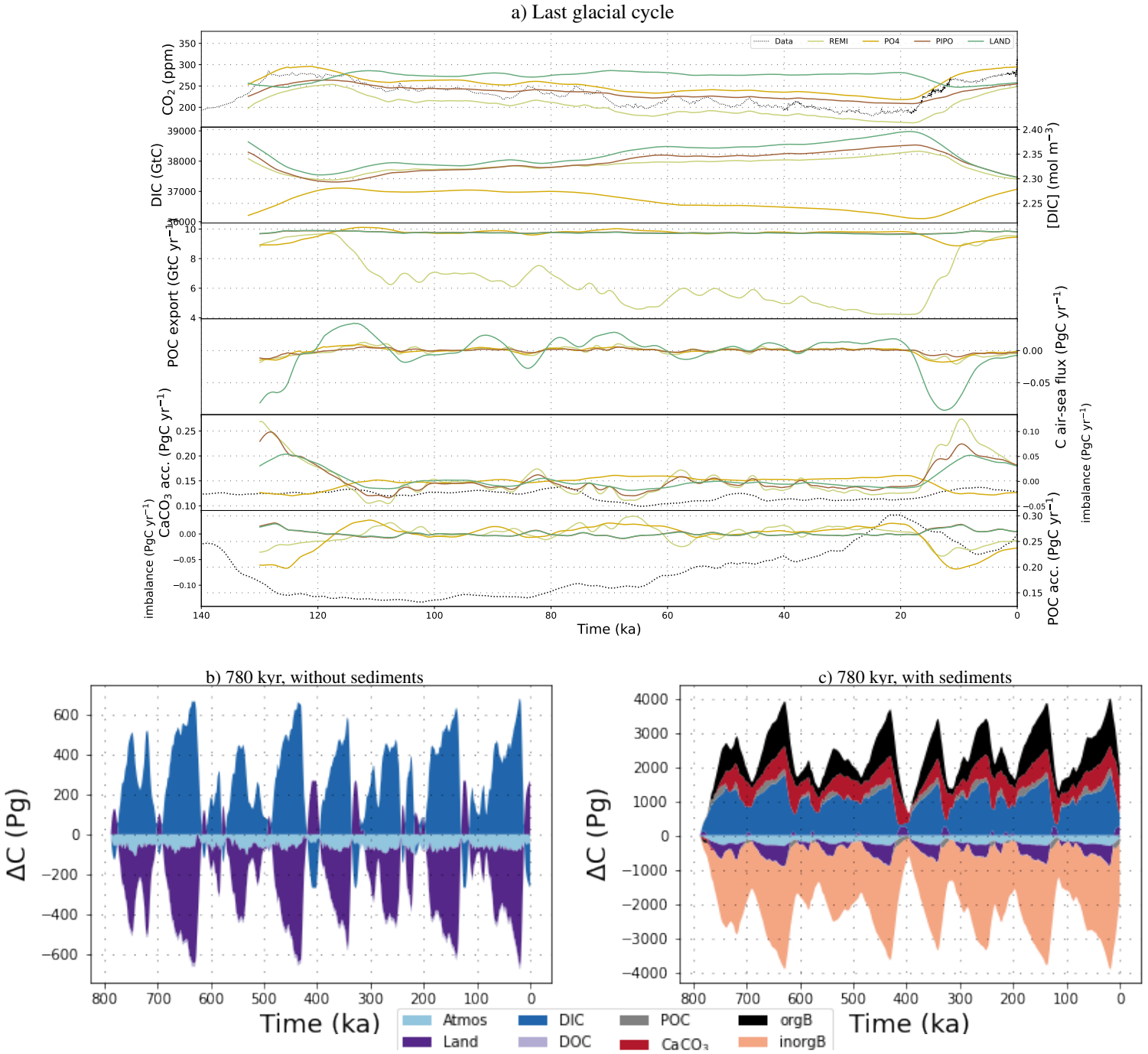

Figure S4. a) Atmospheric CO_2 concentrations, DIC and carbon fluxes over the most recent full glacial cyle in simulations with additional biochemical forcings in an open system. b) Transient carbon reservoir size changes across the last 780 kyr as simulated with all additional biochemical forcings combined in a closed system and c) in an open system. Shown are the size changes of atmospheric, terrestrial, marine (DIC and DOC), sedimentary (POC and $CaCO_3$) and lithospheric (organic and inorganic) carbon storage. Reservoir changes for individual forcings are displayed in Fig S12 and S13. Flux timeseries for simulations in a closed system are displayed in Fig S14.

Biochemical forcings affect carbon transfer primarily through the biological pump and the size of the terrestrial carbon sink. Nutrient inputs during glacial phases in simulation PO4 increase POC and $CaCO_3$ export, and sedimentary burial rates through increased sedimentary mass accumulation and lower O_2 concentrations in the deep ocean (Fig S4). During glacial termination, the prescribed nutrient supply to the surface ocean stops before the deep ocean is fully re-ventilated and the nutrients that accumulated in intermediate and deep water masses have returned to the surface. This delay results in low nutrient concentrations in the surface ocean, a transient drop in POC export, and consequentially burial fluxes. The reduced carbon burial raises DIC and increases the net carbon transfer from surface waters to the atmosphere during deglaciation. In consequence, when nutrients are added to a glacial ocean with responsive sediments, glacial phases become the dominant periods of organic and inorganic C transfer to the lithosphere, reducing the accumulation of marine DIC and increasing the marine uptake of atmospheric CO_2 during glacial phases. This simulation PO4 yields the temporal CO_2 evolution which most closely resembles reconstructions from ice cores.

Reducing the PIC:POC ratio of export production during glacial phases (simulation PIPO) increases alkalinity in the surface ocean which enhances marine carbon uptake from the atmosphere, resulting in an additional CO_2 drawdown of up to $\sim$10ppm without sediments. This effect is enhanced by 20ppm when dynamic sediments are considered. When the export production is tilted towards organic matter production in an ocean with interactive sediments, reduced $CaCO_3$ export during inceptions and glacial periods translate into reduced $CaCO_3$ burial rates. This leads to a shoaling of the carbonate compensation depth, a build-up of alkalinity in the ocean and increased carbon transfer from the atmosphere to the ocean. The reduced sedimentary carbonate accumulation reduces the total mass flux to the sediments. On extratropical continental slopes, the reduced mass accumulation slows organic carbon burial, retaining more nutrients in the ocean and decreasing O_2 concentrations through continued remineralization instead. On continental slopes under upwelling areas with high productivity, the reduced O_2 expands the O_2 minimum zones, an effect which outweighs the local reduction of carbonate export and results in higher POC burial rates despite less carbonate deposition. Restoration of the interglacial PIC:POC ratio during deglaciation then enhances sedimentary carbonate deposition in benthic waters with higher pH and larger O_2 minimum zones than under the standard forcing, increasing the temporal spikes in carbonate and POC burial. Reduced glacial PIC:POC increases $CaCO_3$ burial events during glacial terminations.

Lowering the remineralization depth of organic matter in the glacial water column (simulation REMI) leads to a net carbon and nutrient transfer from the surface ocean to intermediate and deep water masses, where more O_2 is consumed. Without dynamic sediments, the increased DIC concentrations in the deep ocean increases the carbon storage of the glacial ocean. In addition, the reduced dissolution of POC in the upper water column during glacials increases surface ocean pH and CO_2 uptake by the ocean. With dynamic sediments, the resulting reduction in deep ocean O_2 concentration increases POC preservation in sediments below high productivity zones, e.g. tropical continental margins and upwelling areas. Where the larger flux of POC reaching the sediments is not preserved, it is remineralized, reducing the stability of sedimentary $CaCO_3$. Glacial inceptions are then characterized by increased POC and POP fluxes into the sediments and reduced $CaCO_3$ burial. During glacial terminations, POC is increasingly remineralized at shallower depth again, leading to reduced POC fluxes into the deep ocean and POC burial compared to the glacial phase. Surface ocean pH decreases and C is returned to the atmosphere. Compared to the standard

forcing, lowering the remineralization depth thus shifts the timing of maximal POC burial rates from the interglacial to the glacial and amplifies the transient spike in $CaCO_3$ burial as increased nutrient supply during glacials does, but it also increases sedimentary $CaCO_3$ dissolution during glacial phases.

Land carbon release to the atmosphere during glacial phases (simulation LAND) invades and acidifies the ocean due to increased atmospheric concentrations, growing the marine DIC reservoir during glacials with and without dynamic sediments, resulting in the biggest glacial marine DIC reservoirs across our simulations. When interactive sediments are considered, this marine carbon uptake reduces $CaCO_3$ preservation and leads to a shoaling of the lysocline. During termination, as the external carbon addition subsides, the ocean vents carbon back into the atmosphere, transiently allowing for increased $CaCO_3$ burial.

The previous paragraphs show that varying biogenic particle production in the surface ocean is only a relevant control on marine carbon storage changes when interactive sediments are simulated. Instead, lowering the main remineralization depth (simulation REMI) and adding terrestrial carbon release during glaciation (simulation LAND) strongly influence marine carbon storage with and without dynamic sediments. Without dynamic sediments, they double the marine carbon uptake during glacial periods. When including interactive sediments, all biochemical forcings have substantially larger effects on the carbon cycle than physical changes, with 5-10x larger carbon fluxes than under the standard forcing (Fig S4).

CO_2 restoring and non-linear effects of combined forcings on carbon fluxes

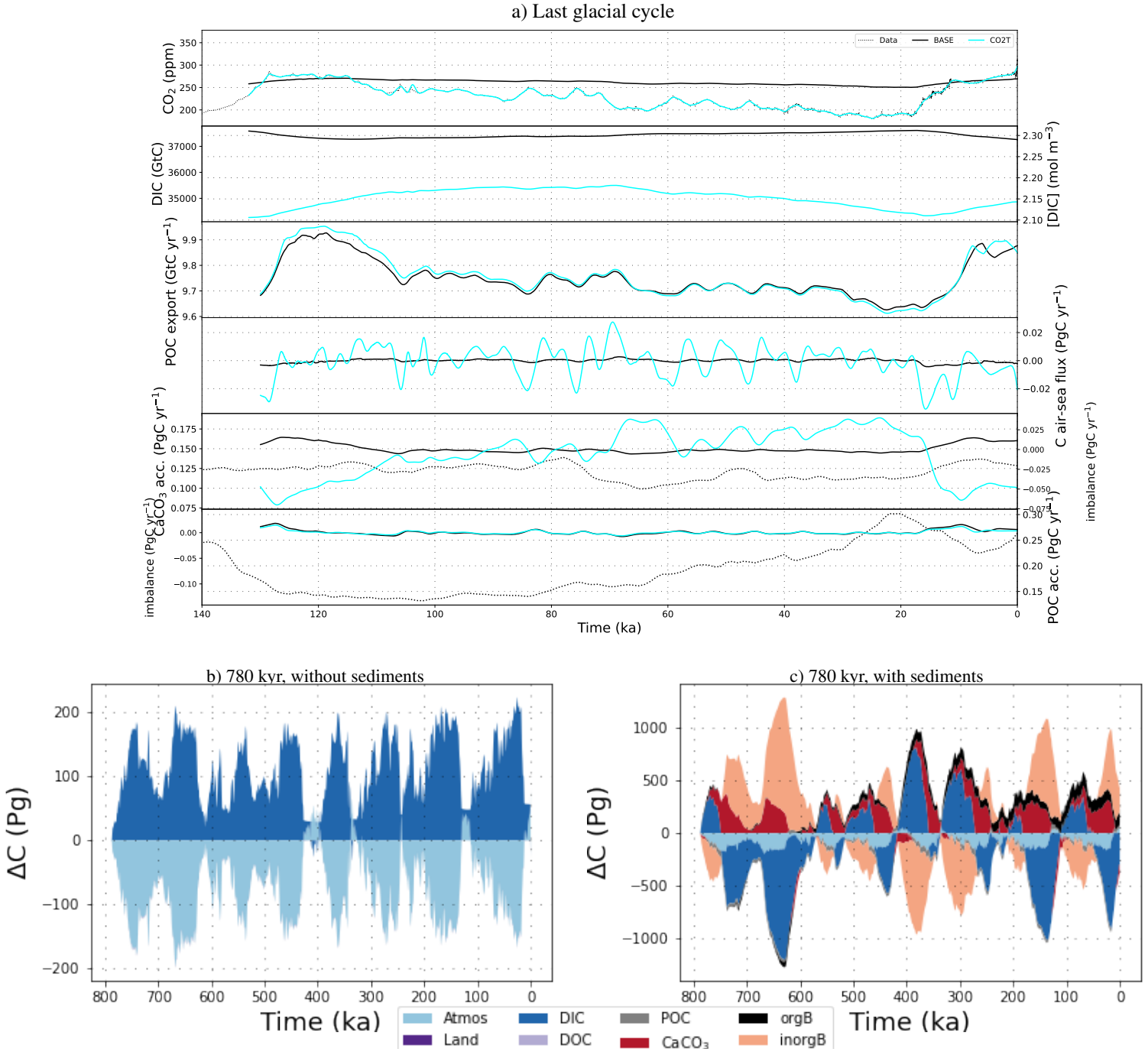

Figure S5. a) Atmospheric CO_2 concentrations, DIC and carbon fluxes over the most recent full glacial cyle in simulations BASE and CO2T in an open system. b) Transient carbon reservoir size changes across the last 780 kyr as simulated with alkalinity nudging in a closed system and c) in an open system. Shown are the size changes of atmospheric, terrestrial, marine (DIC and DOC), sedimentary (POC and $CaCO_3$) and lithospheric (organic and inorganic) carbon storage.

By design, alkalinity nudging causes marine carbon uptake and release that shape atmospheric CO_2 in line with observations (Fig S5). As a consequence, the surface ocean is more alkaline in glacial times and more acidic during terminations than in the standard forcing, enabling increased marine carbon uptake. In simulations with dynamic sediments, $CaCO_3$ burial during cold phases is increased but the burial spike during terminations suppressed.

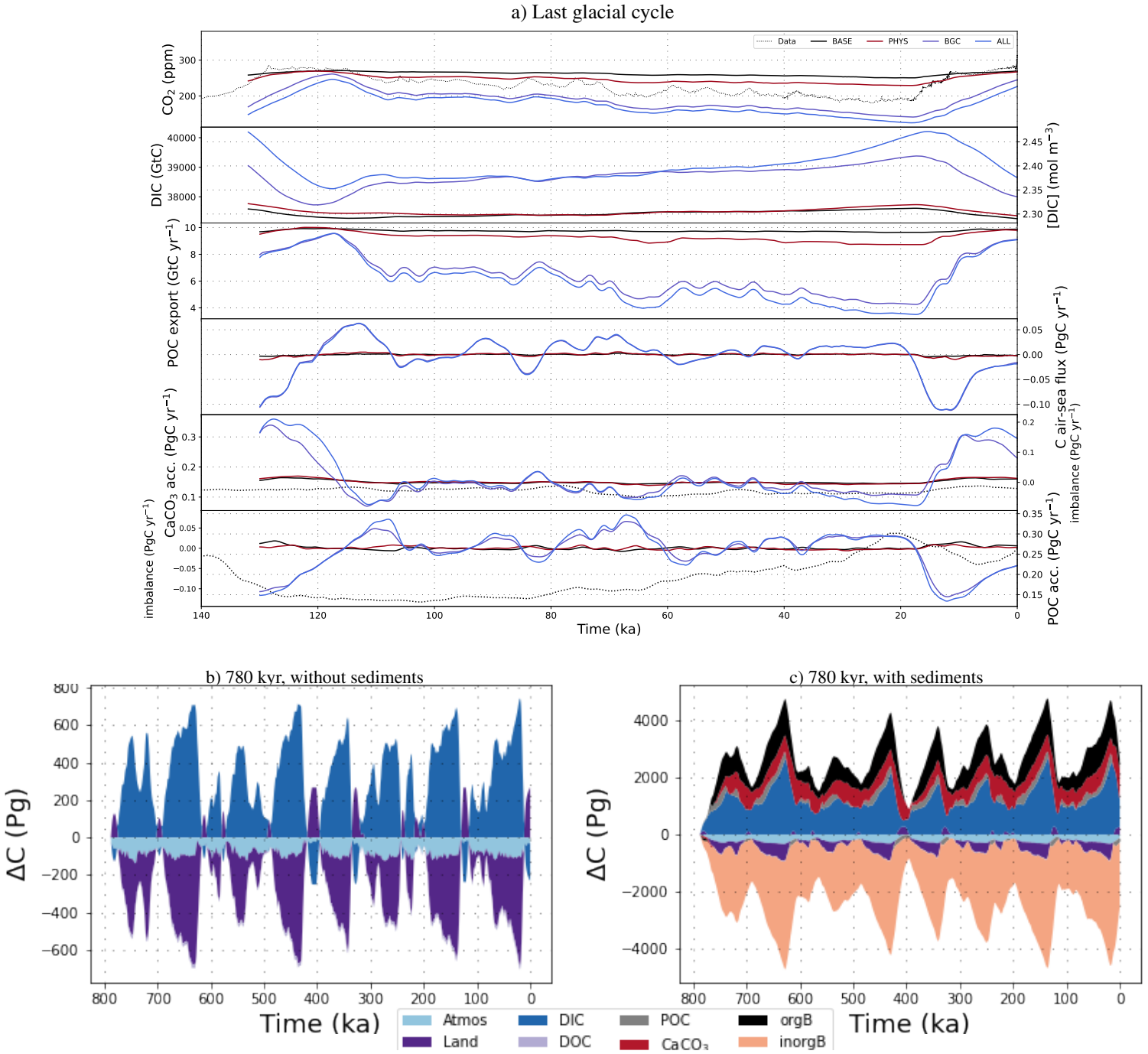

Figure S6. a) Atmospheric CO_2 concentrations, DIC and carbon fluxes over the most recent full glacial cyle in simulations with different combinations of additional forcings in an open system. b) Transient carbon reservoir size changes across the last 780 kyr as simulated with all additional forcings combined in a closed system and c) in an open system. Shown are the size changes of atmospheric, terrestrial, marine (DIC and DOC), sedimentary (POC and $CaCO_3$) and lithospheric (organic and inorganic) carbon storage. Flux timeseries for simulations in a closed system are displayed in Fig S15.

The three tested physical forcings combine almost linearly in their effect on atmospheric CO_2. Circulation change is dominated by radiation reductions, with strong AMOC weakening during glacials and some reduction of the PMOC, but less than in simulation SOWI because of increased sea ice cover in the Southern Ocean which limits the effect of wind stress changes. In consequence, the glacial deep ocean holds more nutrients when all forcings are combined: it has a large Atlantic reservoir due to sluggish overturning and a larger Pacific reservoir than in SOWI due to less organic carbon burial. During deglaciation, the release of these nutrients back into the surface ocean creates a larger productivity spike than when the forcings are applied individually, reducing marine [O_2] further but causing only a minimal temporary reduction of <5 ppm in atmospheric CO_2 (Fig. S6). In simulations with interactive sediments, additional radiative forcing (AERO) and Southern Ocean wind forcing (SOWI) shift sedimentary $CaCO_3$ and POC accumulation rates in opposite directions. Yet, their effects on nutrient, temperature and oxygen distributions are almost additive.

While physical effects on carbon concentrations combine almost linearly, the combination of biochemical forcings is non-linear because they directly alter production and dissolution patterns in opposing ways. Acidification of benthic water masses through external nutrient (PO4) and carbon (LAND) supply during glacials counteracts the benthic pH increase under a deepened remineralisation depth (REMI). When all biochemical forcings are combined, net $CaCO_3$ fluxes into marine sediments are reduced during glacial maxima and increased during terminations, but the burial peak is delayed. Biochemical forcings dominate the carbon cycle response when all forcings are combined, except for the North Atlantic where circulation changes cause the biggest perturbation. The magnitude of the non-linearities that occur when all forcings are combined is similar to the combined effect of only the physical forcings.

Climate feedback effects

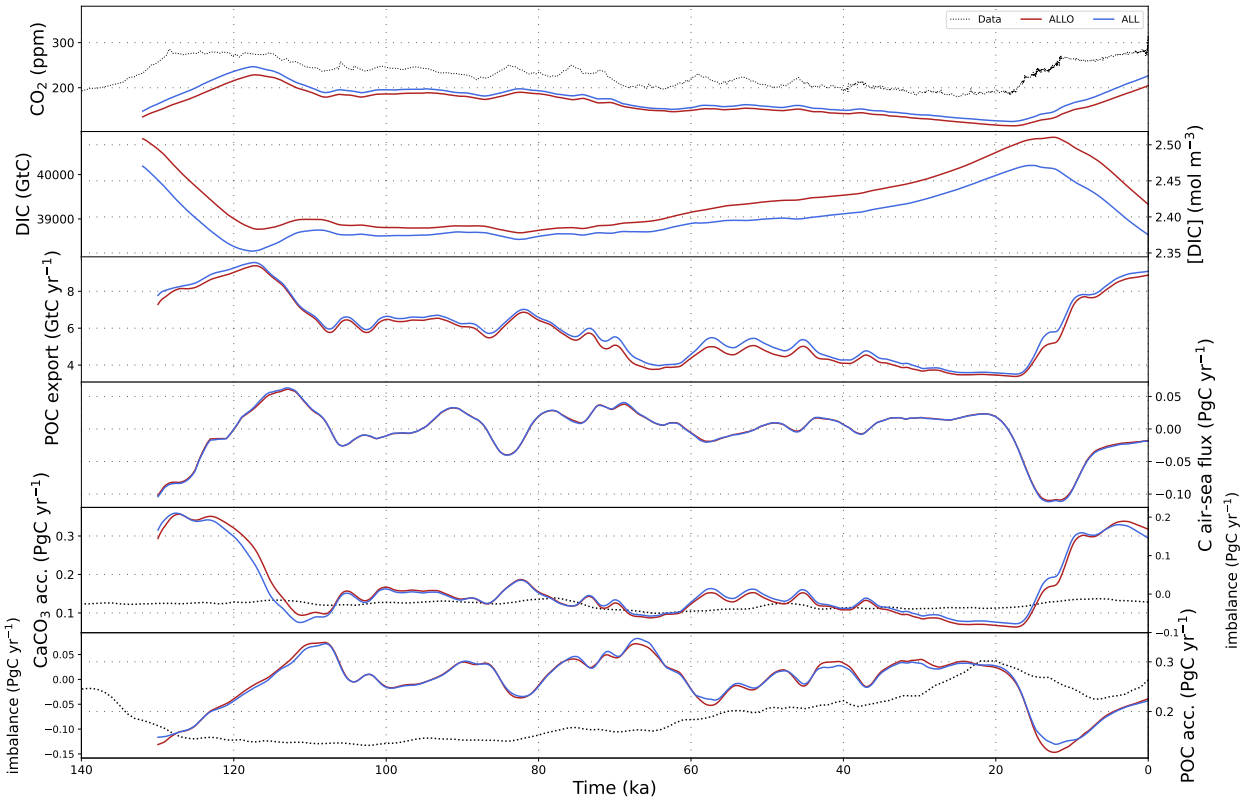

Figure S7. Atmospheric CO_2 concentrations, DIC and carbon fluxes over the most recent full glacial cyle in simulations with all additional forcings combined in an open system, with and without climate feedback.

All simulations described so far were run with prescribed radiative forcing, i.e. without the radiative effect of simulated CO_2 changes. The benefit of this setup is that the climatic changes in the simulations are comparable, allowing to distinguish the carbon cycle effects of temperature change from the other physical and biochemical changes we simulated. At the same time, however, this simplified setup creates a bias by neglecting the climate feedback of carbon cycle changes. To assess the effect of this bias in the prescribed carbon cycle dynamics, we reran simulation ALL, which contains all tested forcings, with the carbon cycle climate feedback (ALL-Clim). The prescribed forcings in simulation ALL result in a glacial-interglacial CO_2 change that is 30% larger than in observations, but with absolute CO_2 values mostly below those reconstructed. Including the radiative effect of this CO_2 offset results in up to 2.5° colder glacial maxima. Simulation AERO showed that cooling has only limited effects on the carbon cycle. The additional cooling increases marine CO_2 uptake and reduces primary productivity, and consequently the amount of $CaCO_3$ and POC reaching the sediments, during glacial phases. The climate response to the simulated carbon cycle changes thus causes a net C and nutrient transfer into the ocean, increasing the peak glacial-interglacial atmospheric CO_2 difference by 10 ppm.

Additional Figures

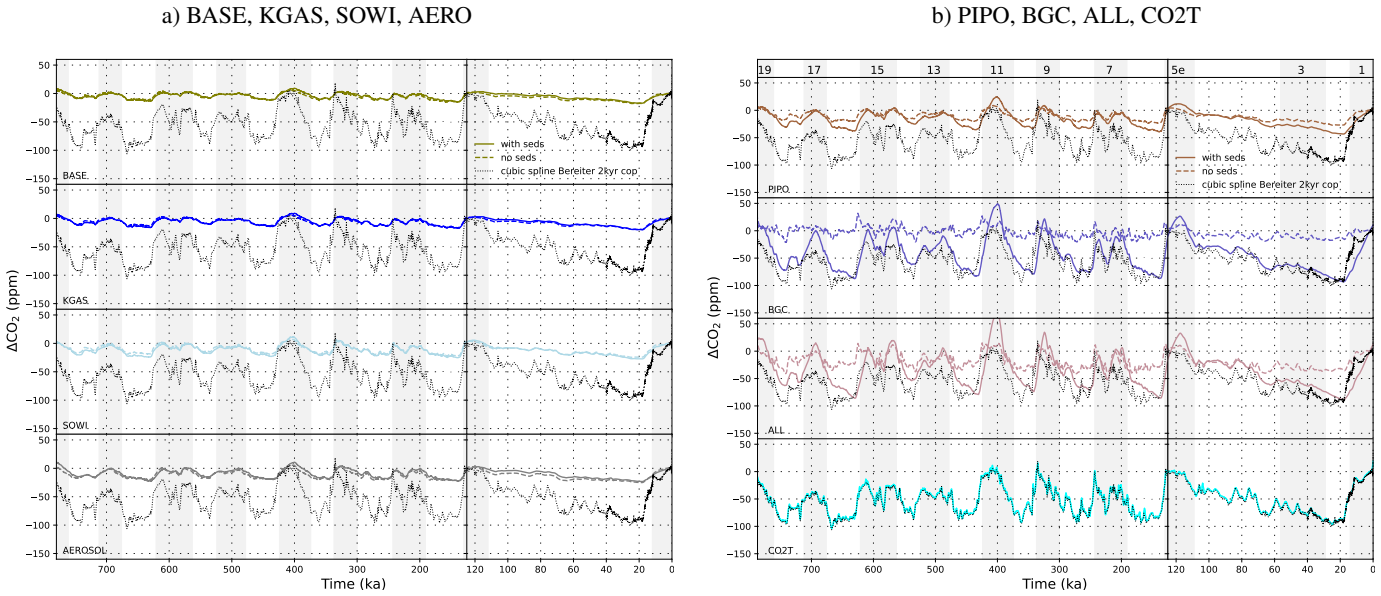

Figure S8. Transient variations of atmospheric CO_2 concentrations as simulated in the simulations not shown in Fig. 2 in the main text, and as reconstructed by Bereiter et al. (2015). Shown is the deviation from the respective pre-industrial value.

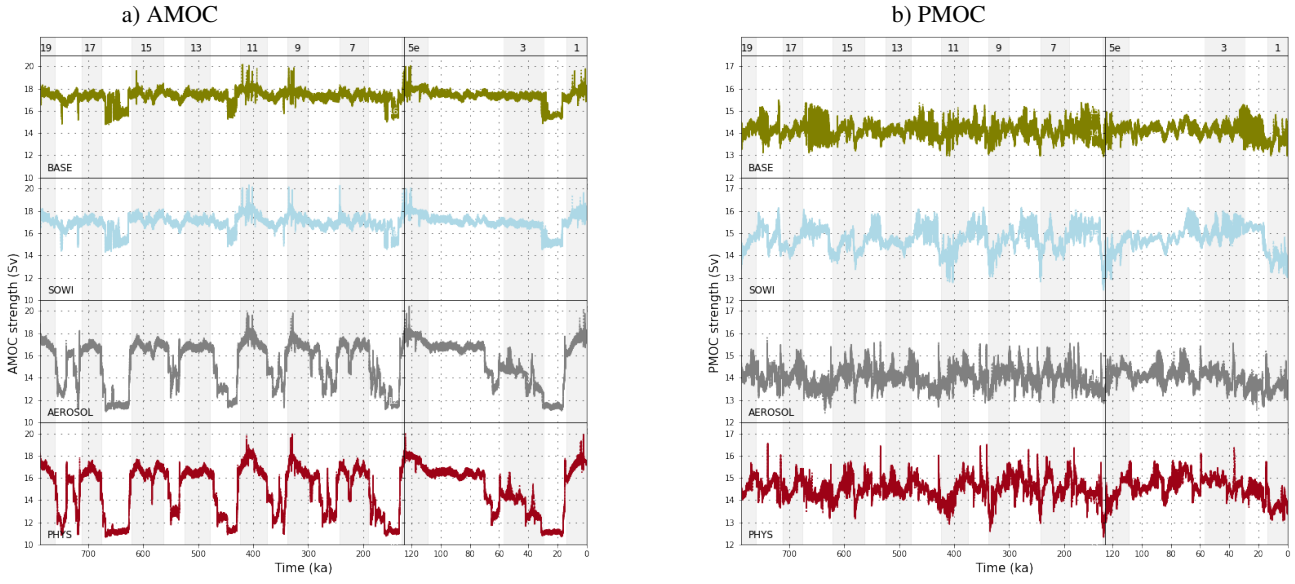

Figure S9. Transient variations of AMOC and PMOC strengths in simulations with different physcial forcings.

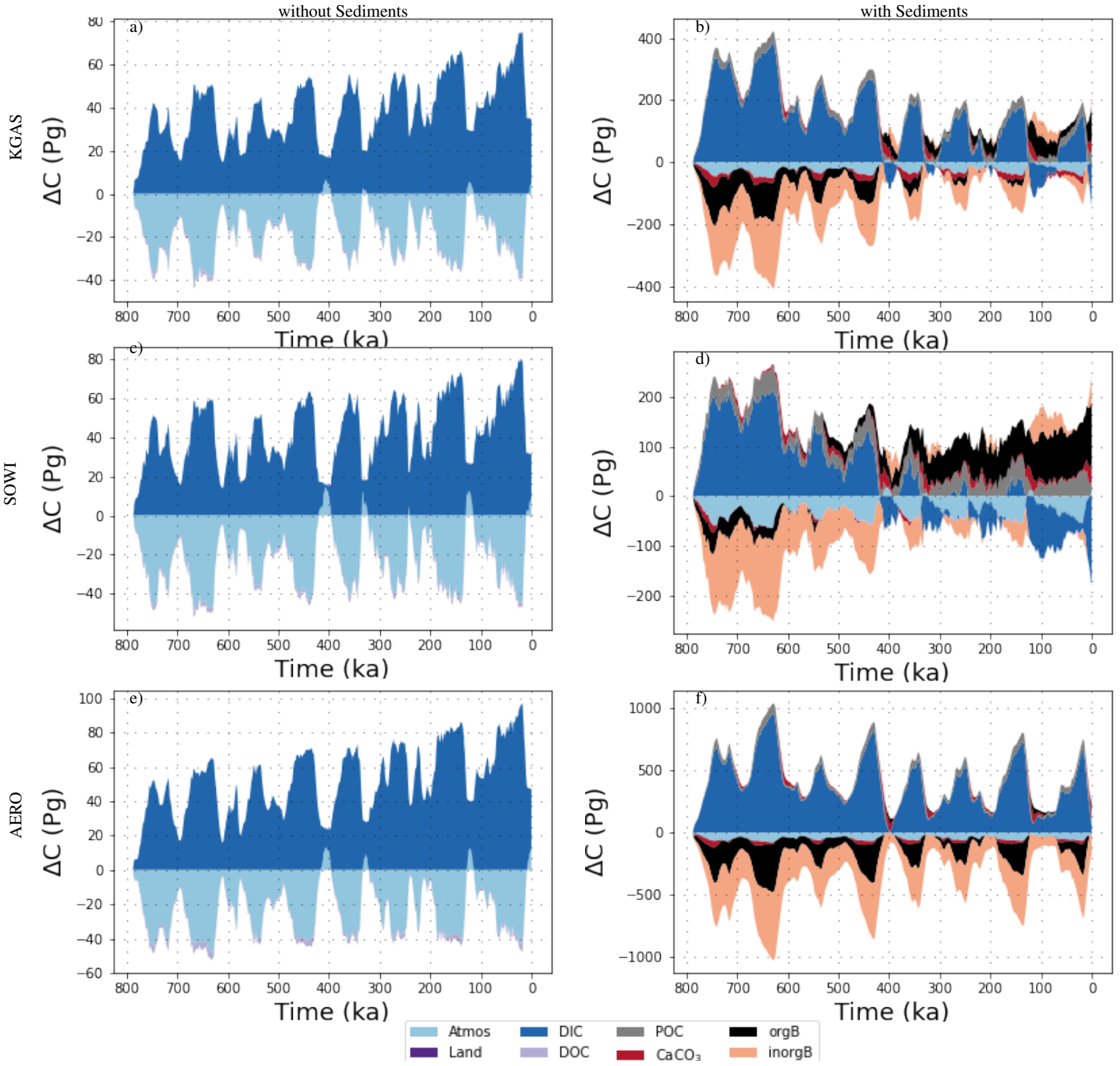

Figure S10. Transient carbon reservoir size changes across the last 780 kyr as simulated in simulations with the standard forcings plus additional physical forcings, left in a closed and right in an open system. Shown are the size changes of atmospheric, terrestrial, marine (DIC and DOC), sedimentary (POC and $CaCO_3$) and lithospheric (organic and inorganic) carbon storage.

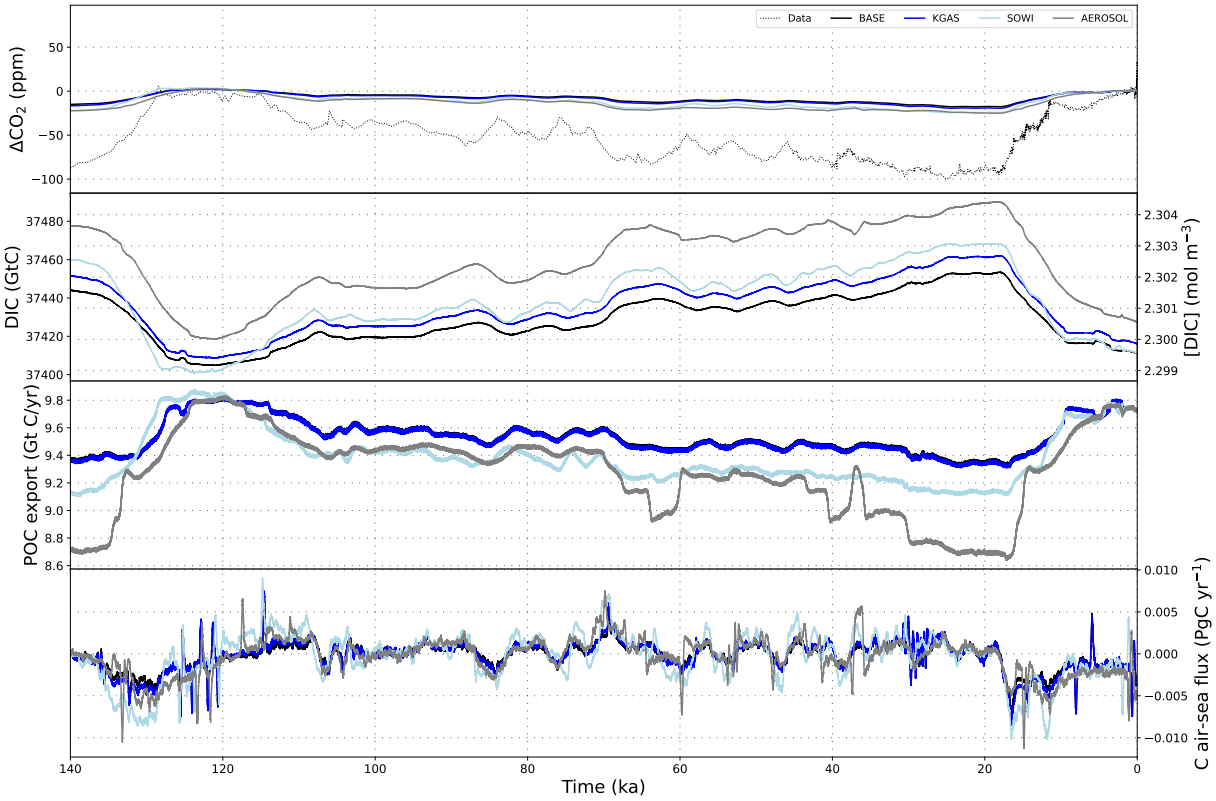

Figure S11. Atmospheric CO_2 concentrations, DIC and carbon fluxes over the most recent full glacial cyle in simulations with additional physical forcings and without dynamic sediments.

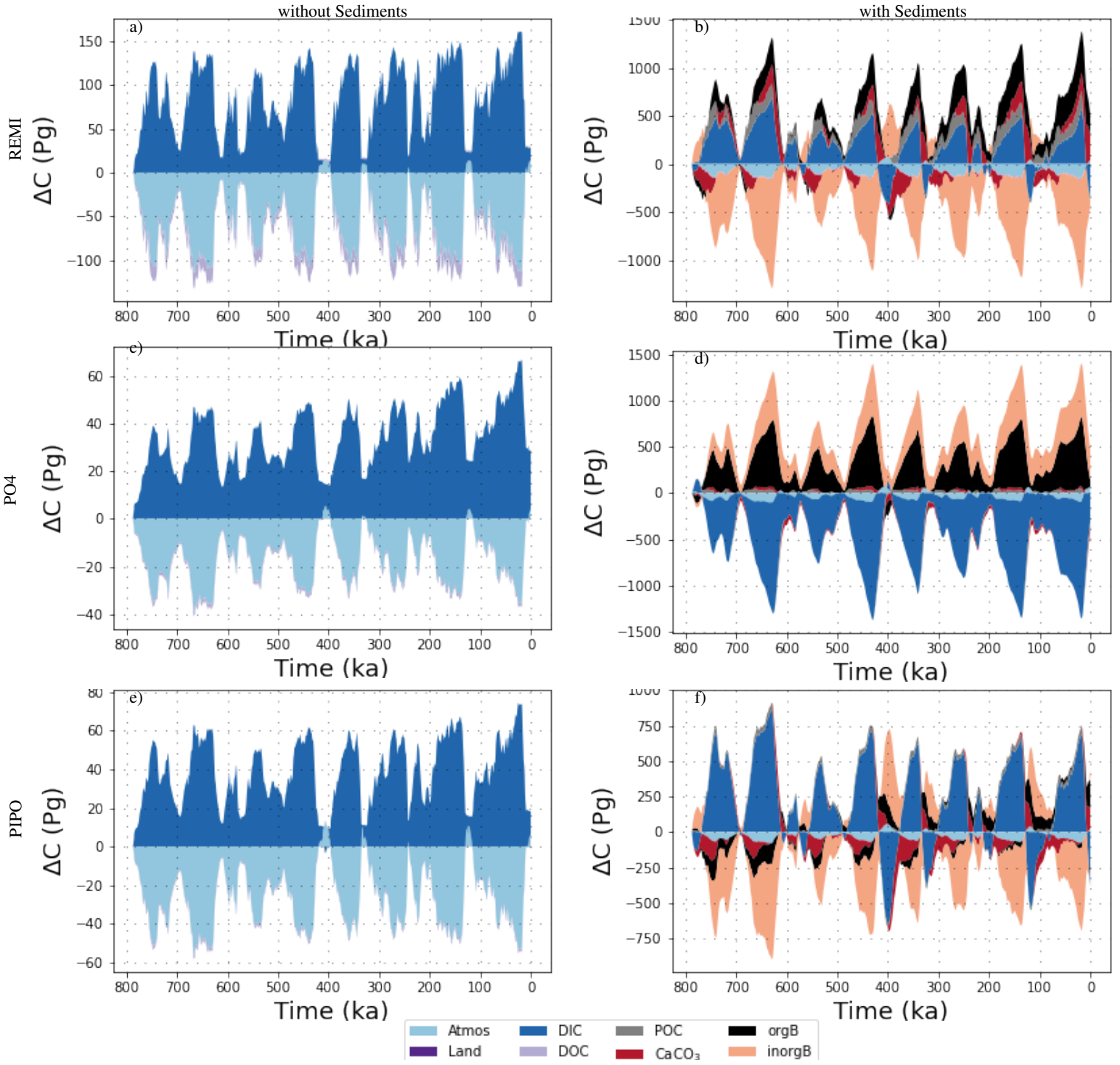

Figure S12. Transient carbon reservoir size changes across the last 780 kyr as simulated in simulations with the standard forcings plus additional biochemical forcings, left in a closed and right in an open system. Shown are the size changes of atmospheric, terrestrial, marine (DIC and DOC), sedimentary (POC and $CaCO_3$) and lithospheric (organic and inorganic) carbon storage.

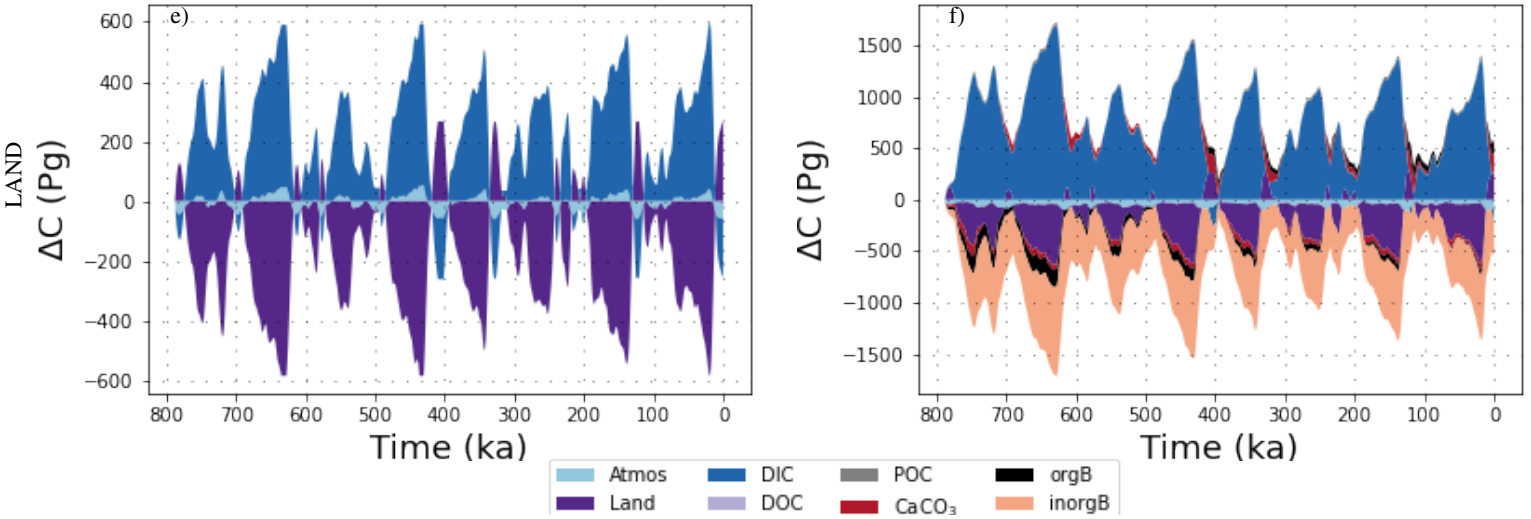

Figure S13. Transient carbon reservoir size changes across the last 780 kyr as simulated in simulations with the standard forcings plus terrestrial C fluxes, left in a closed and right in an open system. Shown are the size changes of atmospheric, terrestrial, marine (DIC and DOC), sedimentary (POC and $CaCO_3$) and lithospheric (organic and inorganic) carbon storage.

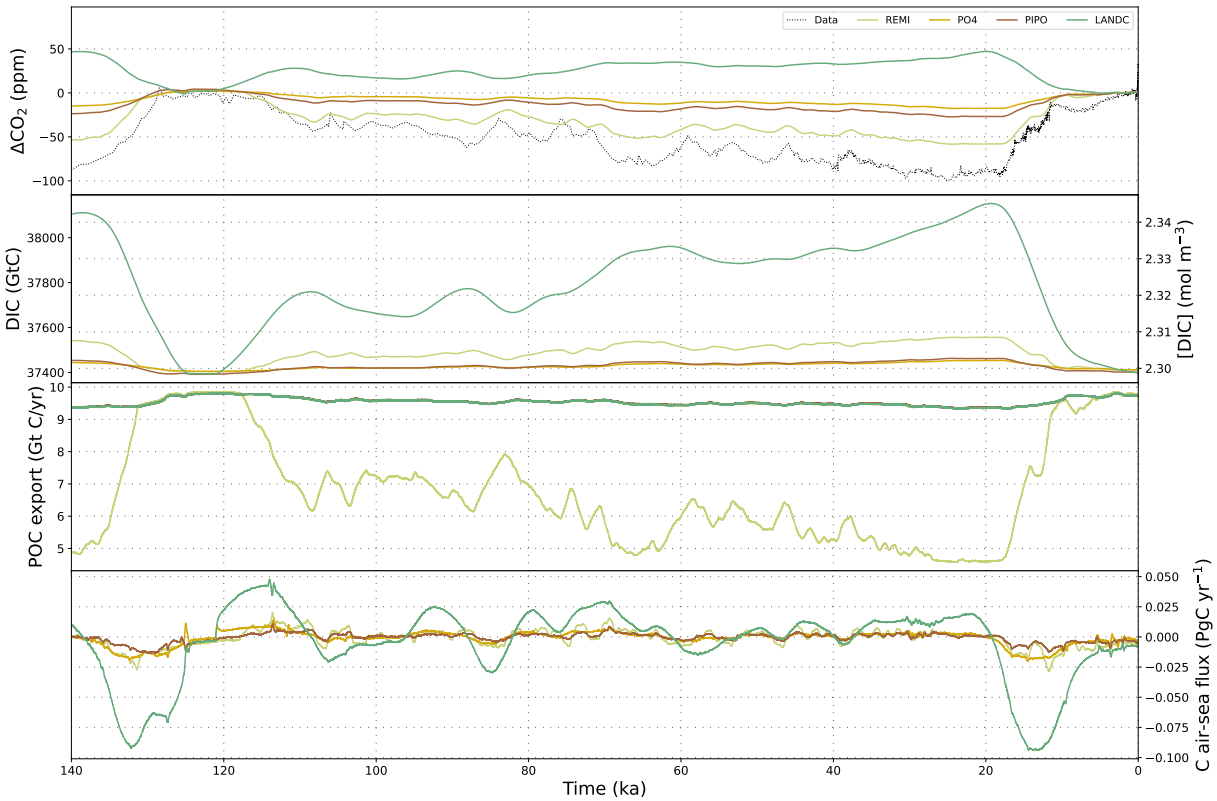

Figure S14. Atmospheric CO_2 concentrations, DIC and carbon fluxes over the most recent full glacial cyle in simulations with additional biochemical forcings and without dynamic sediments.

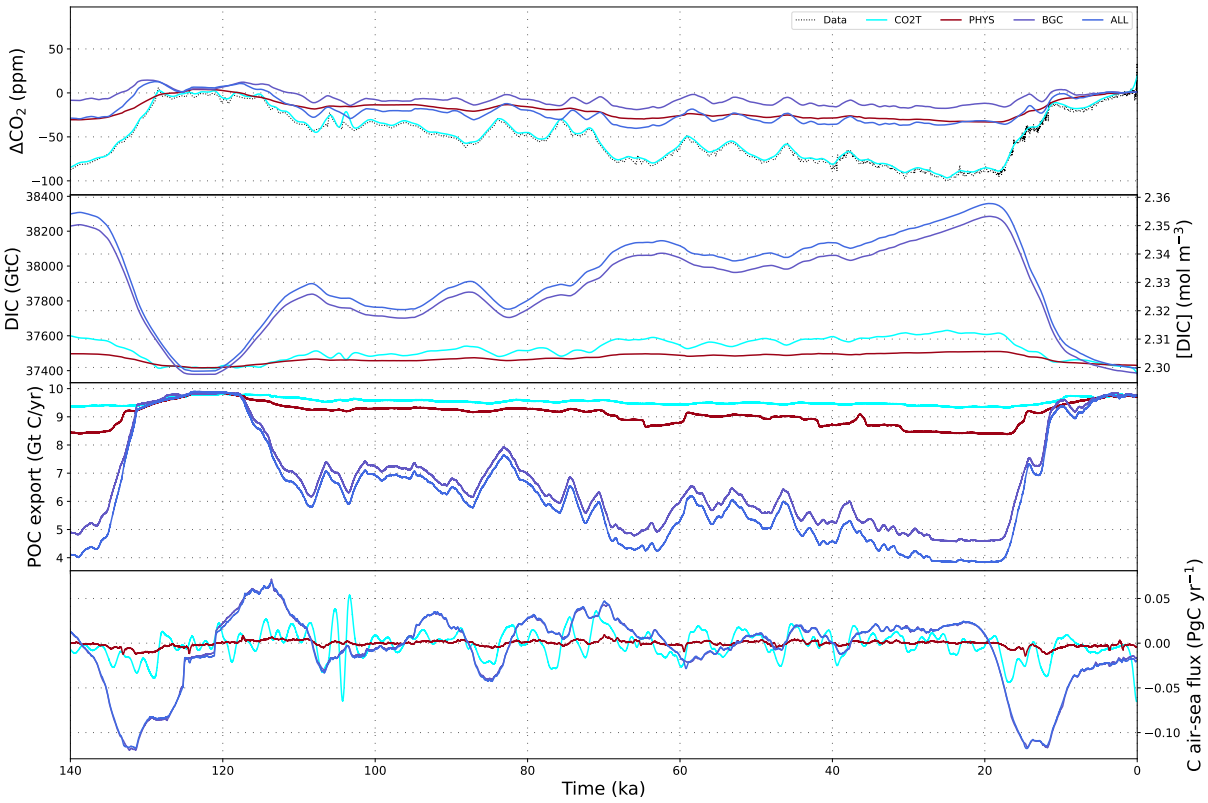

Figure S15. Atmospheric CO_2 concentrations, DIC and carbon fluxes over the most recent full glacial cyle in simulations with combinations of additional forcings and without dynamic sediments.

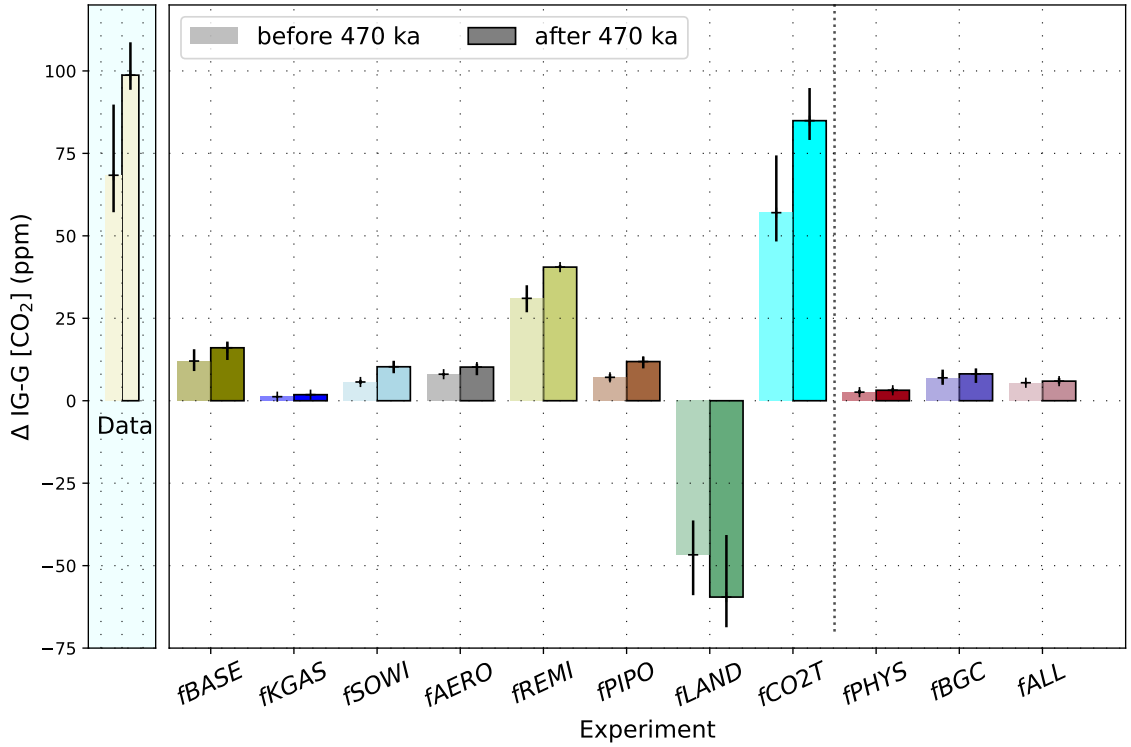

Figure S16. Difference of the glacial-interglacial atmospheric CO_2 amplitude before and after the MBT in our simulations without interactive sediments compared to that in the reconstructed CO_2 record (Bereiter et al., 2015, , horizontal black line).

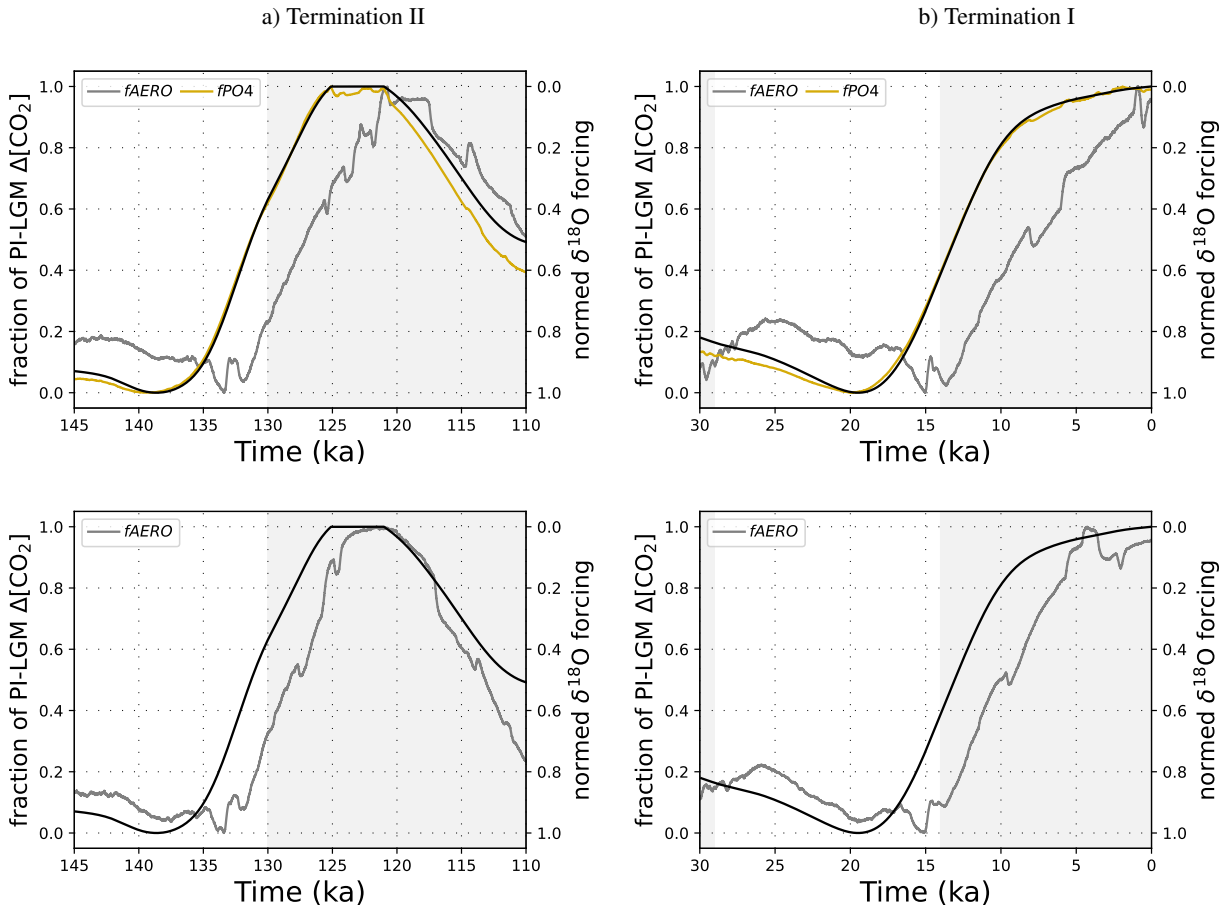

Figure S17. δ^{18}O-derived scaling of the prescribed forcing and the resulting simulated atmospheric CO_2, normalized by the respective PI-LGM CO_2 difference, in selected simulations with interactive sediments (top row) and without interactive sediments (bottom row).

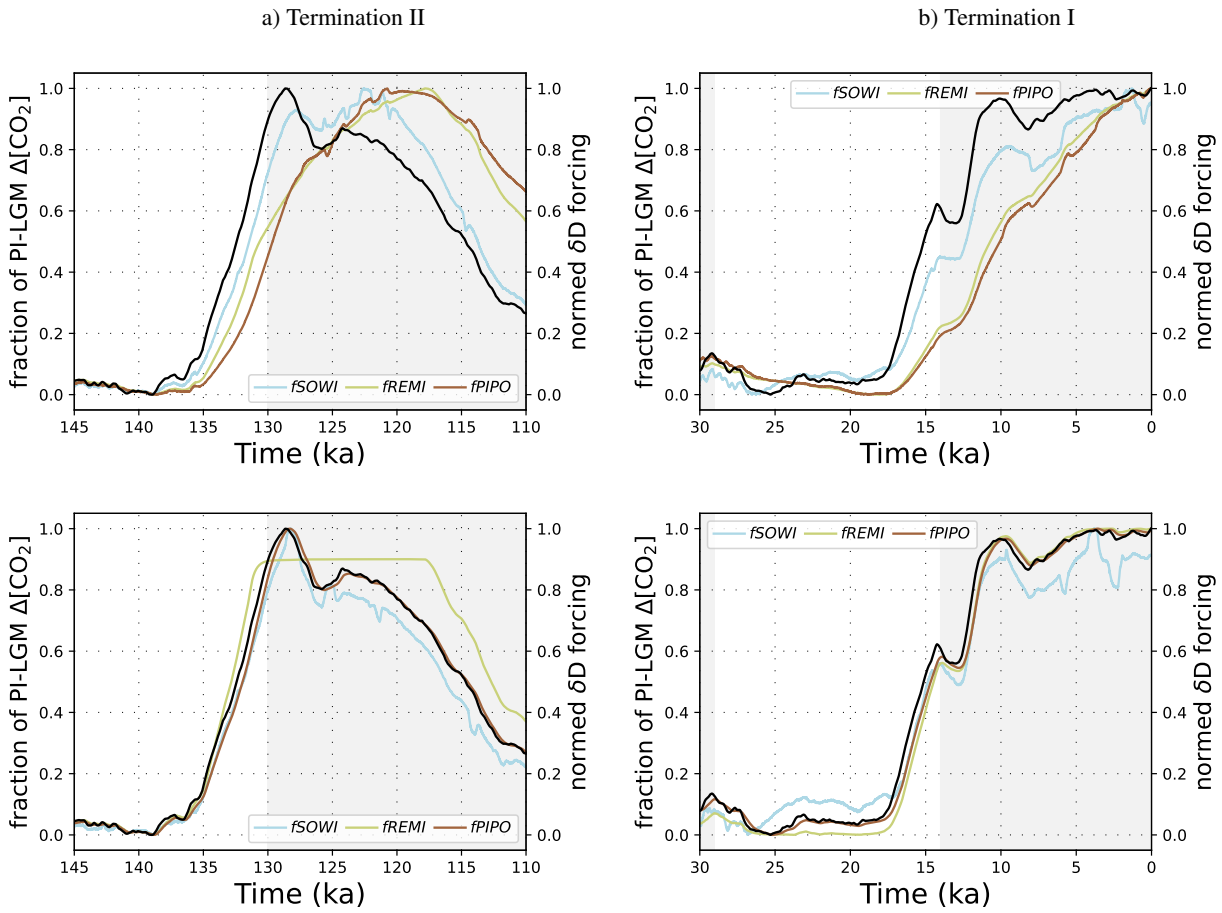

Figure S18. δD-derived scaling of the prescribed forcing and the resulting simulated atmospheric CO_2, normalized by the respective PI-LGM CO_2 difference, in selected simulations with interactive sediments (top row) and without interactive sediments (bottom row).

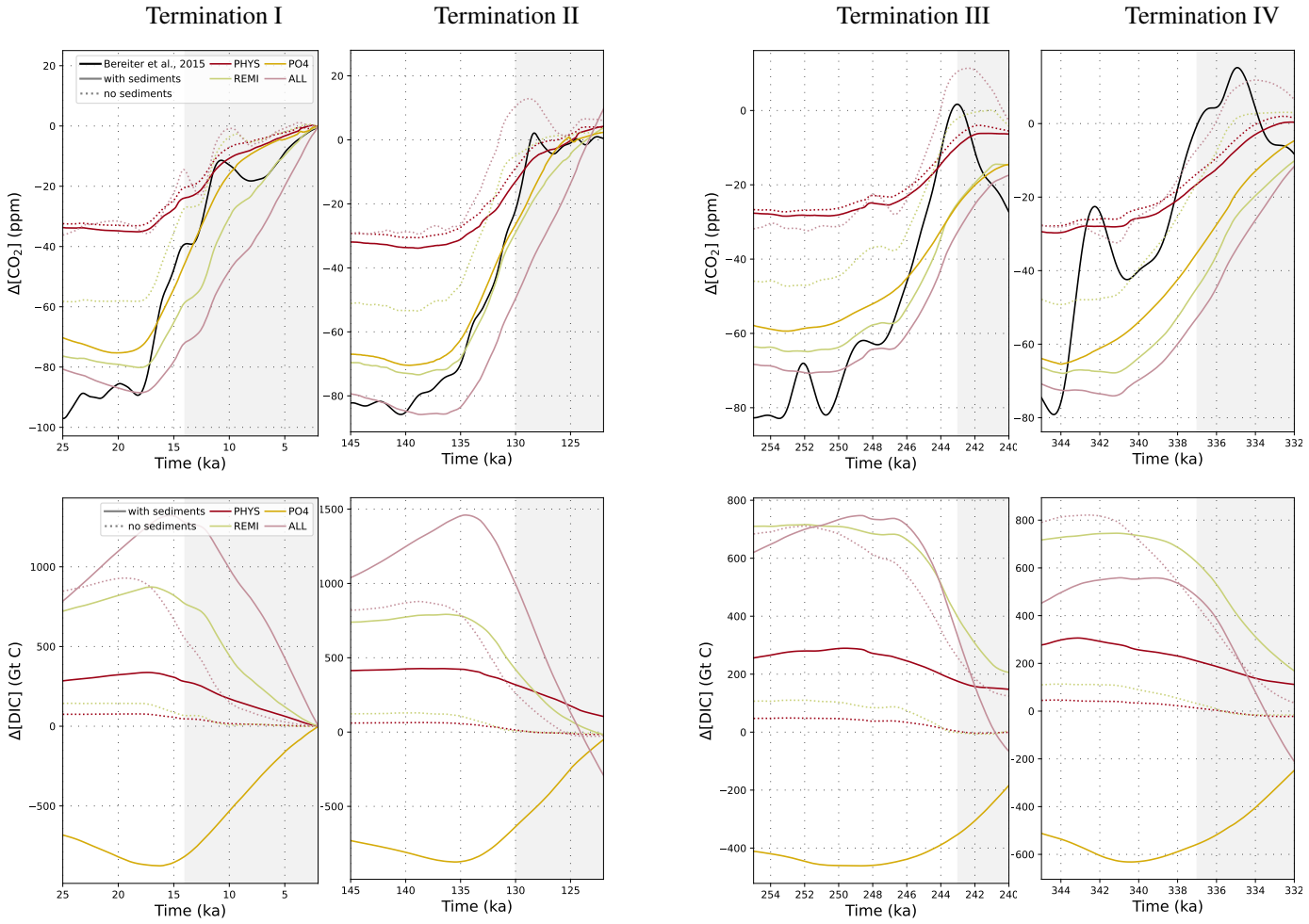

Figure S19. Reconstructed and simulated atmospheric CO_2 changes (upper row) and simulated DIC changes (lower row) across the last four deglaciations.

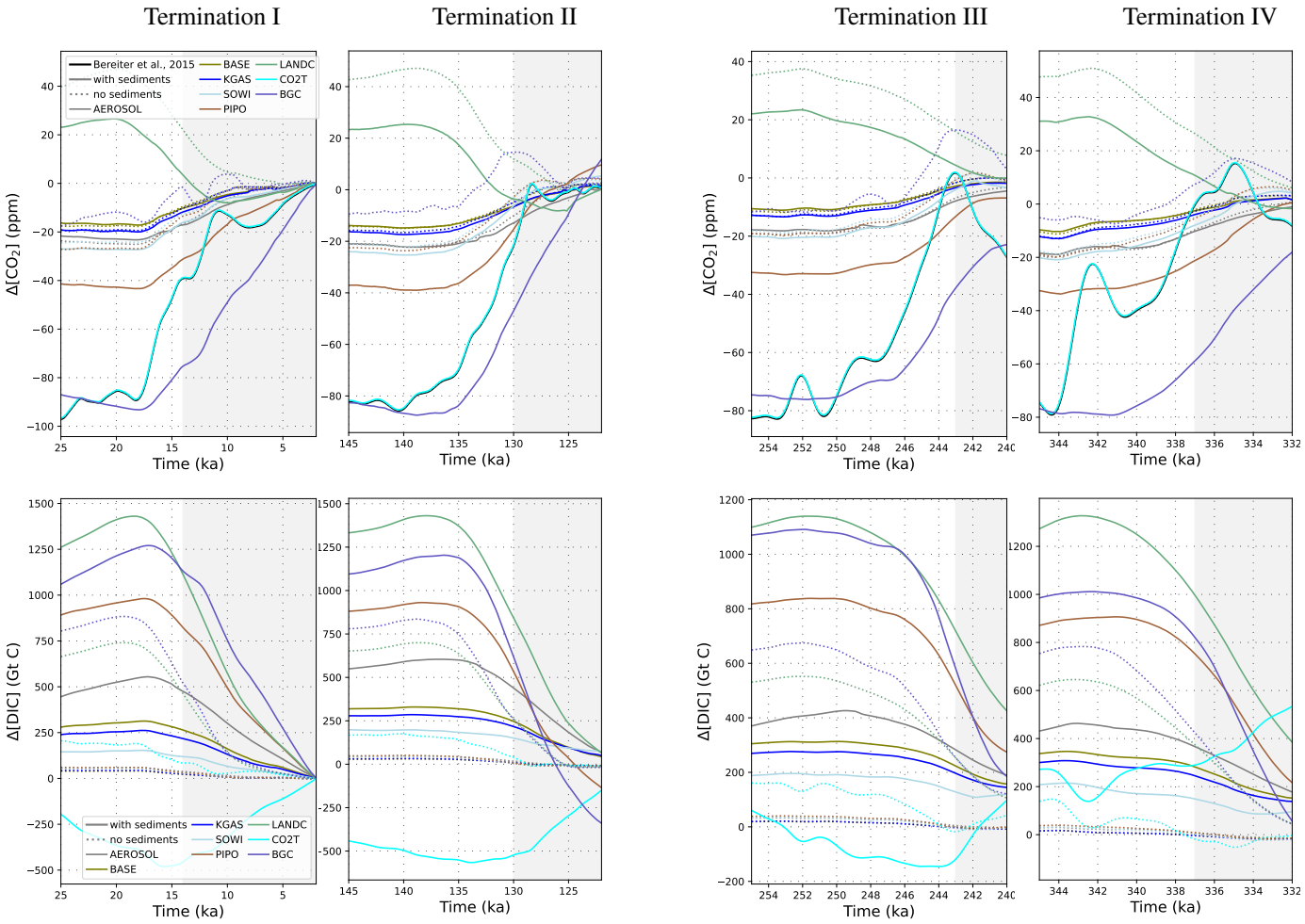

Figure S20. Reconstructed and simulated atmospheric CO_2 changes (upper row) and simulated DIC changes (lower row) across the last four deglaciations.

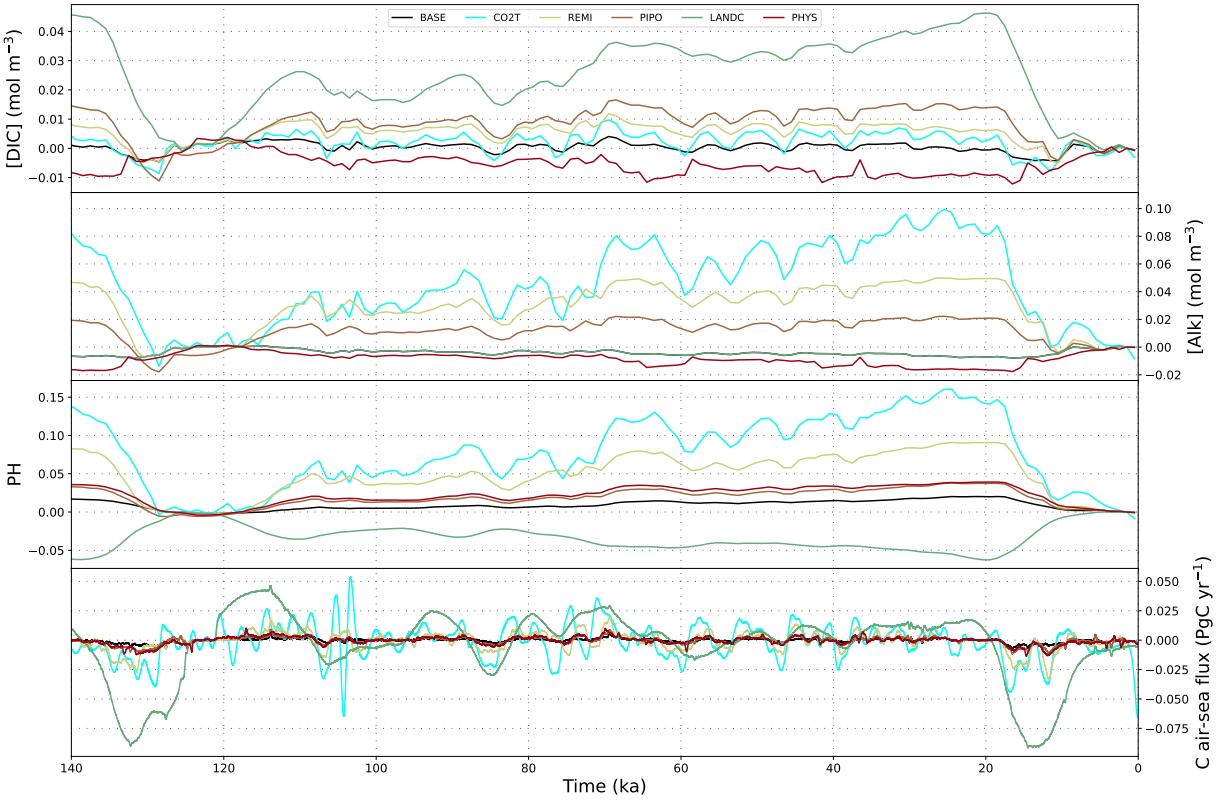

Figure S21. Globally-averaged changes in surface ocean carbonate system parameters in selected simulations without interactive sediments.

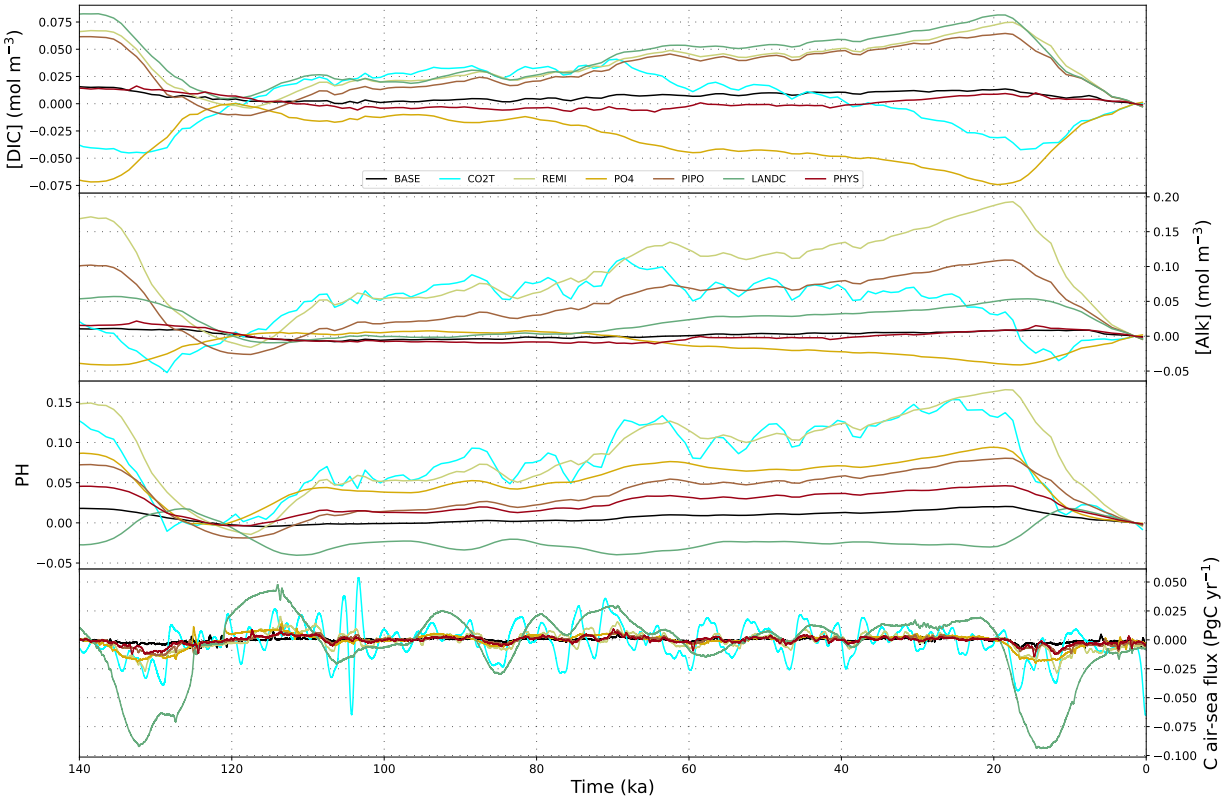

Figure S22. Globally-averaged changes in surface ocean carbonate system parameters in selected simulations with interactive sediments.

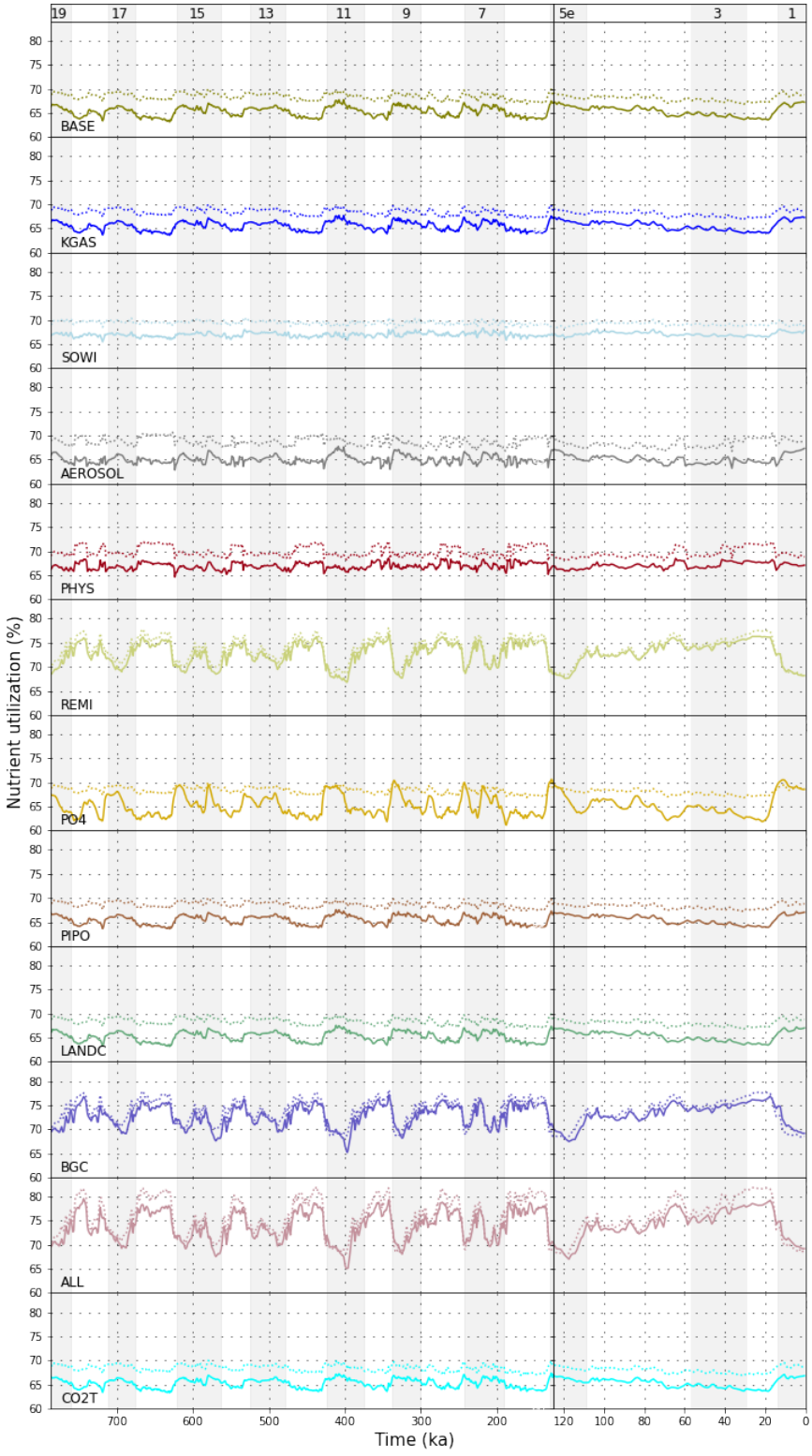

Figure S23. Globally-averaged changes in nutrient utilization in the surface ocean across the simulated 780 kyr.

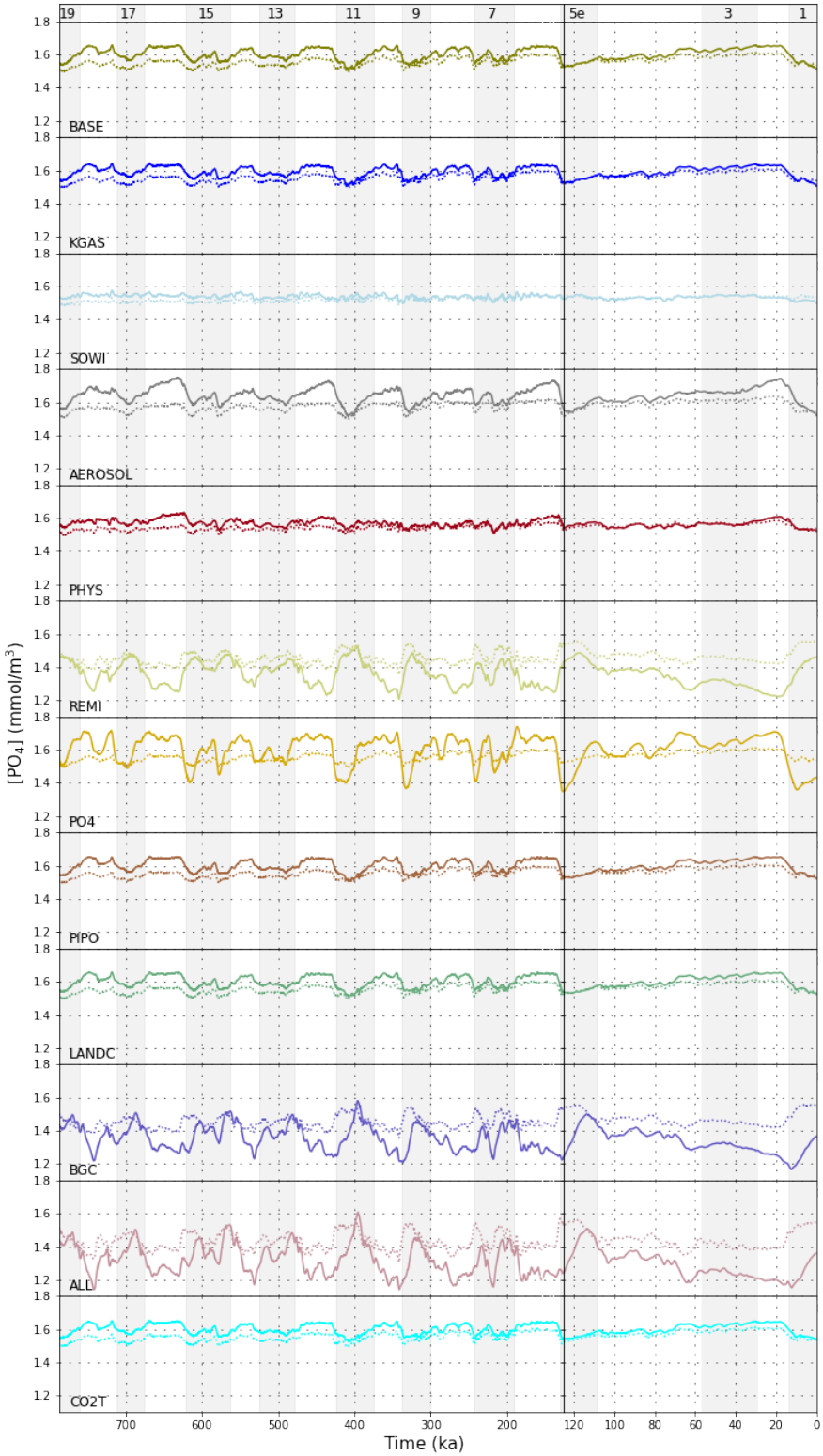

Figure S24. Globally-averaged changes in $PO_{4,pre}$ concentrations across the simulated 780 kyr.

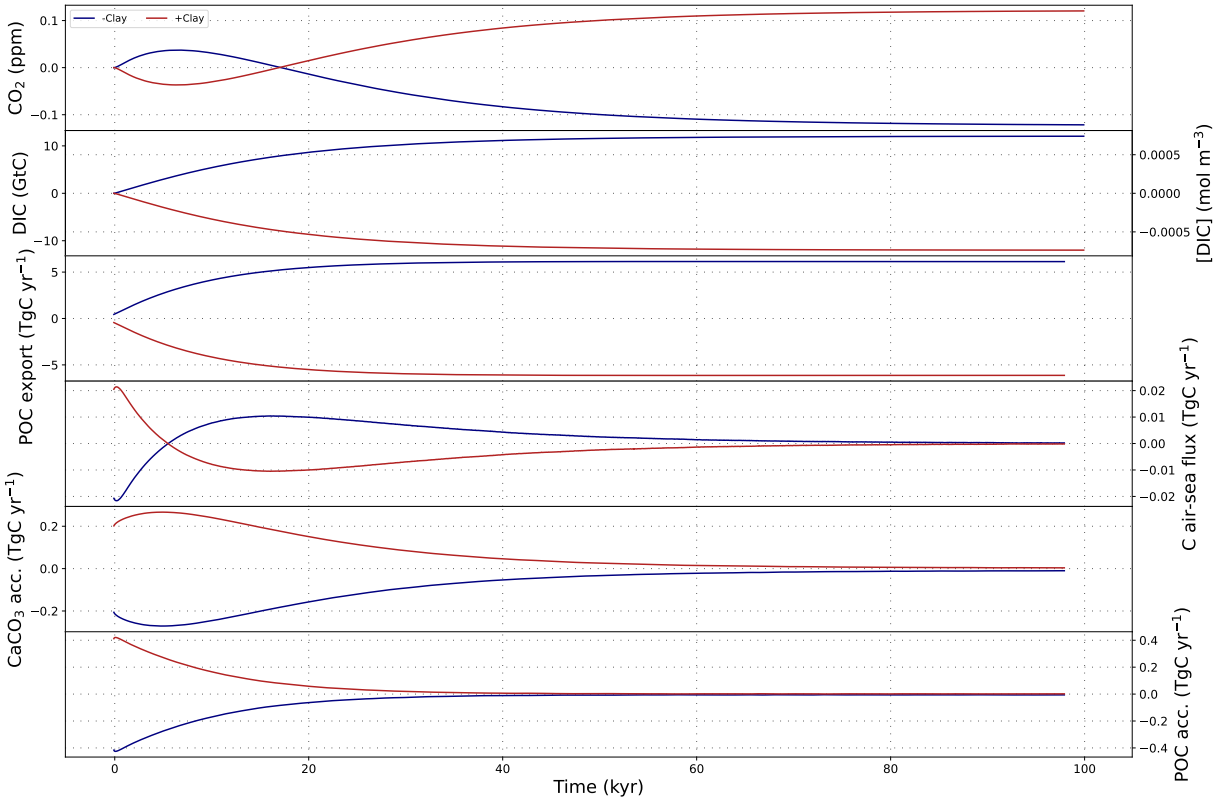

Figure S25. The effect of step changes of plus or minus 30% of the prescribed clay flux on atmospheric CO_2 concentrations, DIC and carbon fluxes over 100 kyr.

a) 120 ka - 20 ka

b) 20 ka - PI

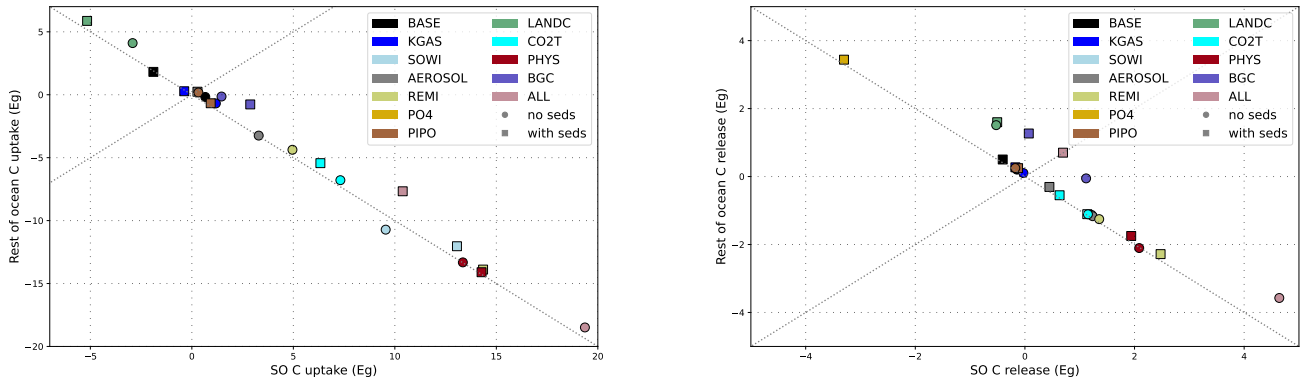

Figure S26. Marine net carbon uptake during the last glaciation (a) and net carbon release during the last deglaciation (b) in the Southern Ocean (>40 °C) compared to the rest of the ocean.

a) $fCO2T$, $fKGAS$, $fSOWI$, $fAERO$

b) $fPIPO$, $fLAND$, $fBGC$, $fALL$

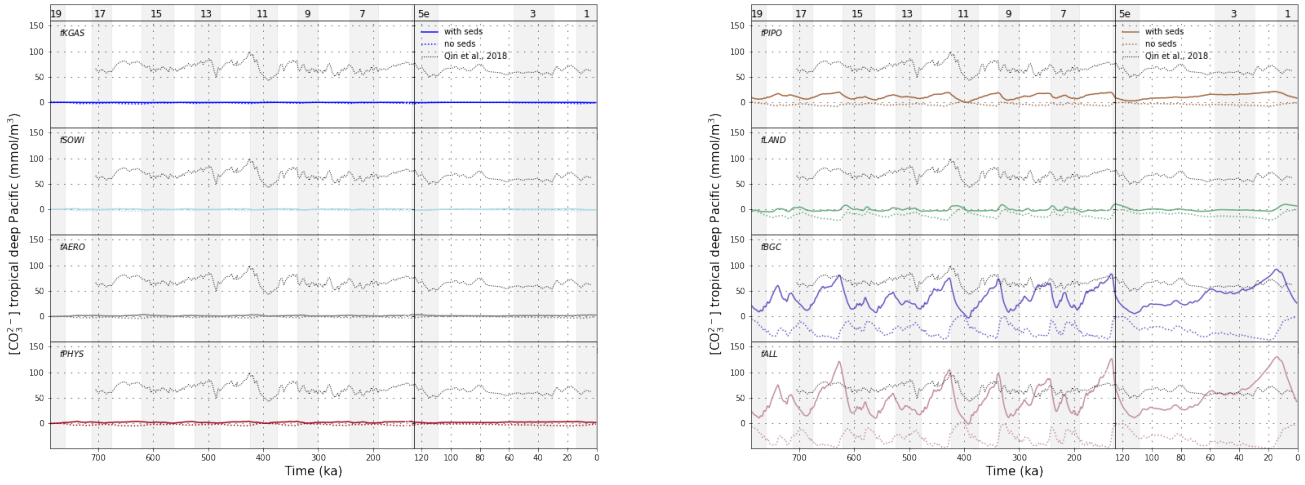

Figure S27. Transient variations of $[CO_3^{2-}]$ in the tropical deep Pacific as simulated in simulations and reconstructed by Qin et al. (2018).

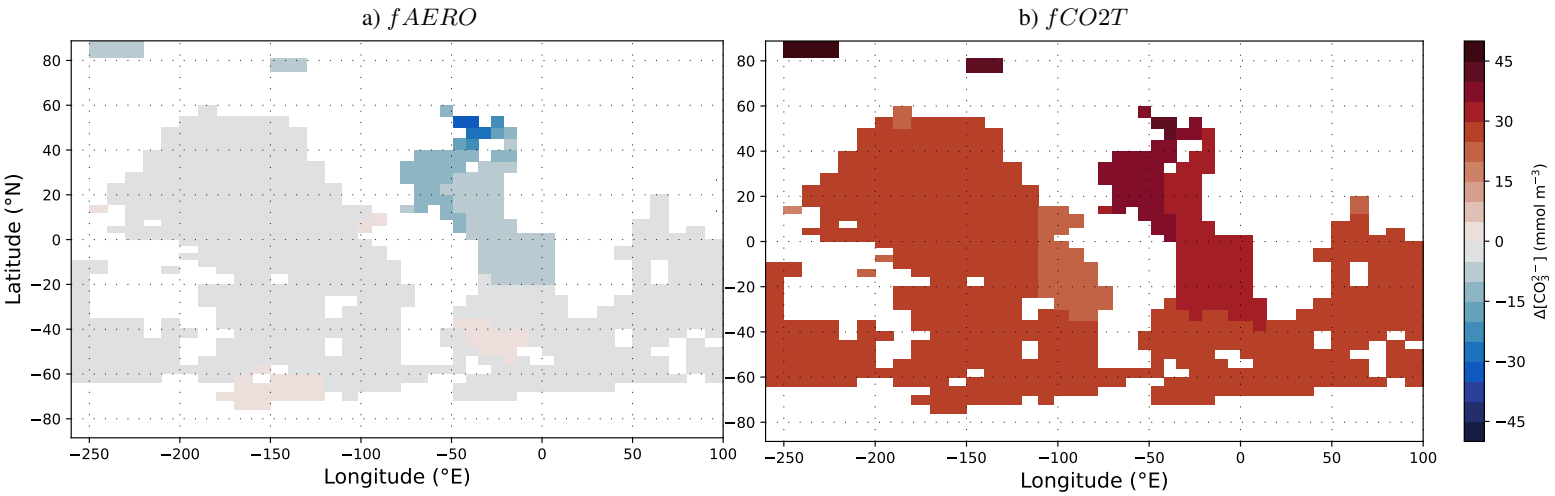

Figure S28. Selected factorial effects on simulated LGM-PI differences in deep CO_3^{2-} (3500 m depth).

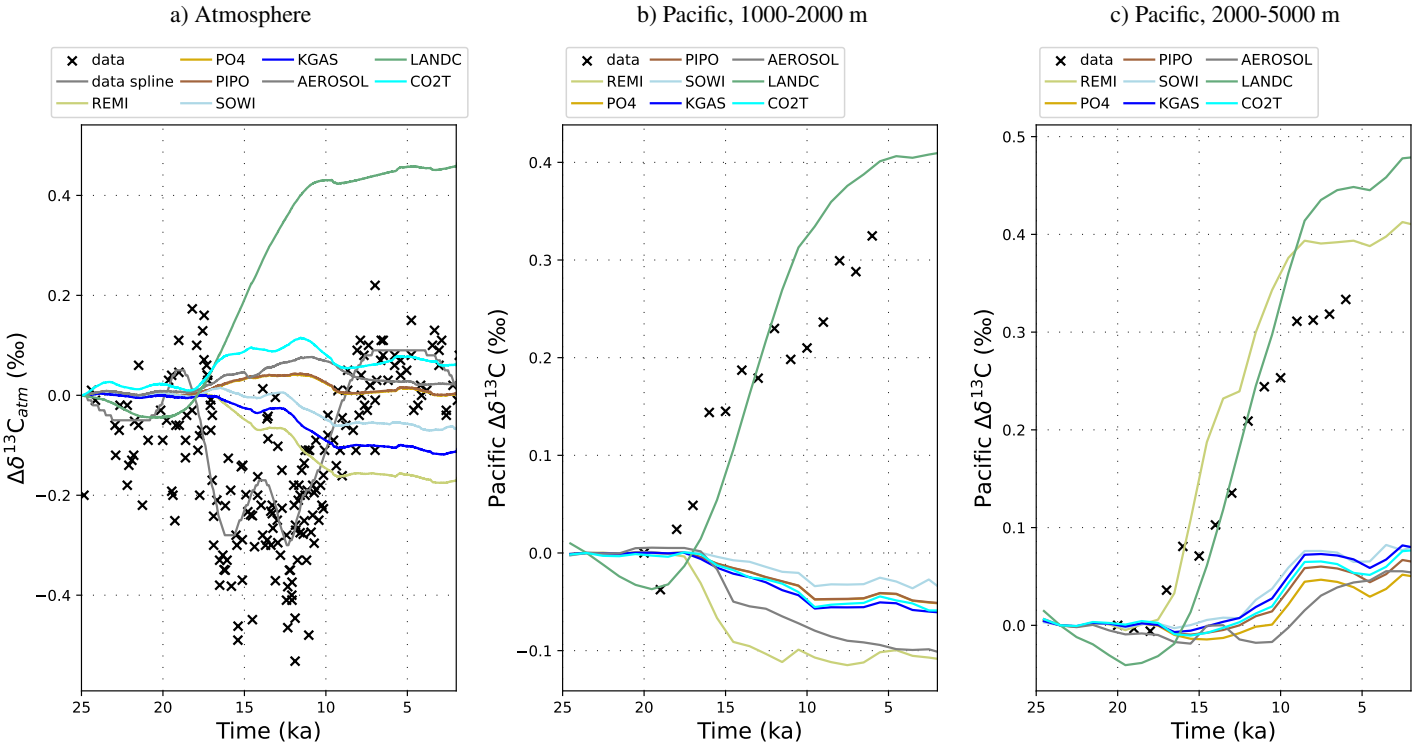

Figure S29. $\delta^{13}C$ changes over the last deglaciation in the atmosphere, intermediate and deep Pacific ocean. Full lines are the results of simulations with a closed system. The data points are reconstructions from Schmitt et al. (2012), Eggleston et al. (2016) and Peterson and Lisiecki (2018).

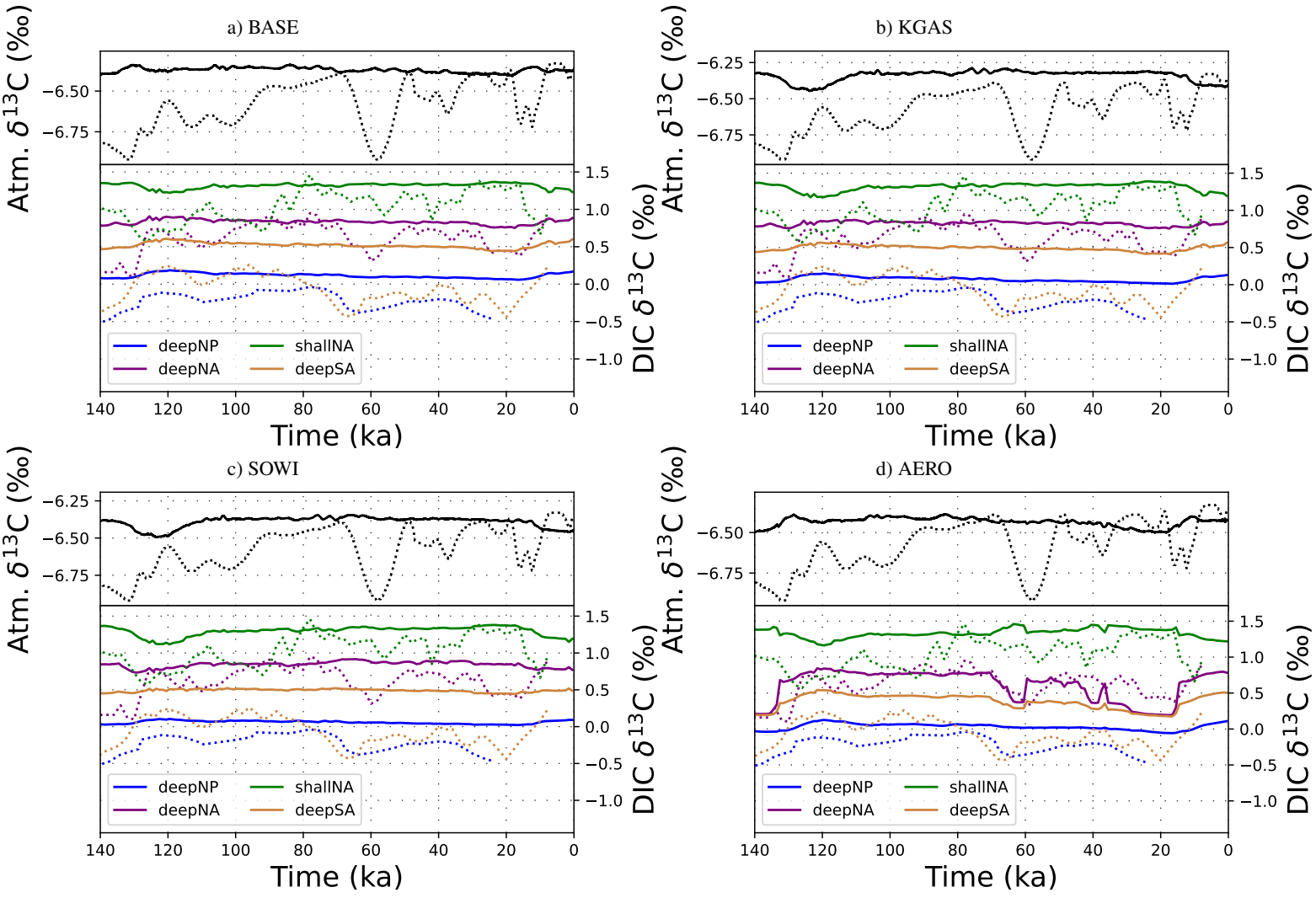

Figure S30. δ^{13}C over the most recent glacial cycle in various reservoirs. Full lines are simulation results with different physical forcings in an open system, dotted lines are reconstructions from Köhler et al., 2010, Eggleston et al., 2016 and Barth et al., 2020

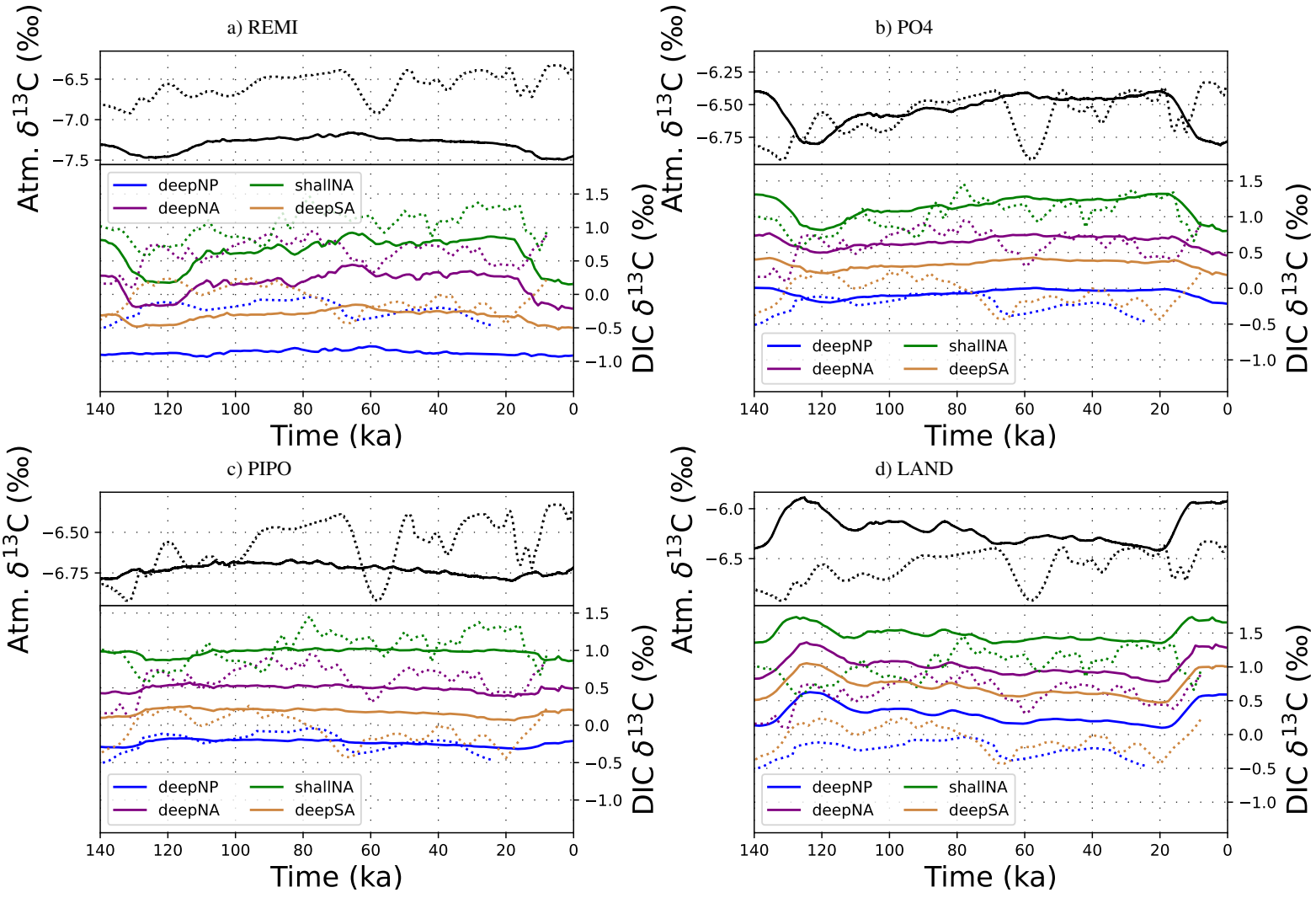

Figure S31. δ^{13}C over the most recent glacial cycle in various reservoirs. Full lines are simulation results with different biochemical forcings in an open system, dotted lines are reconstructions from Köhler et al., 2010, Eggleston et al., 2016 and Barth et al., 2020

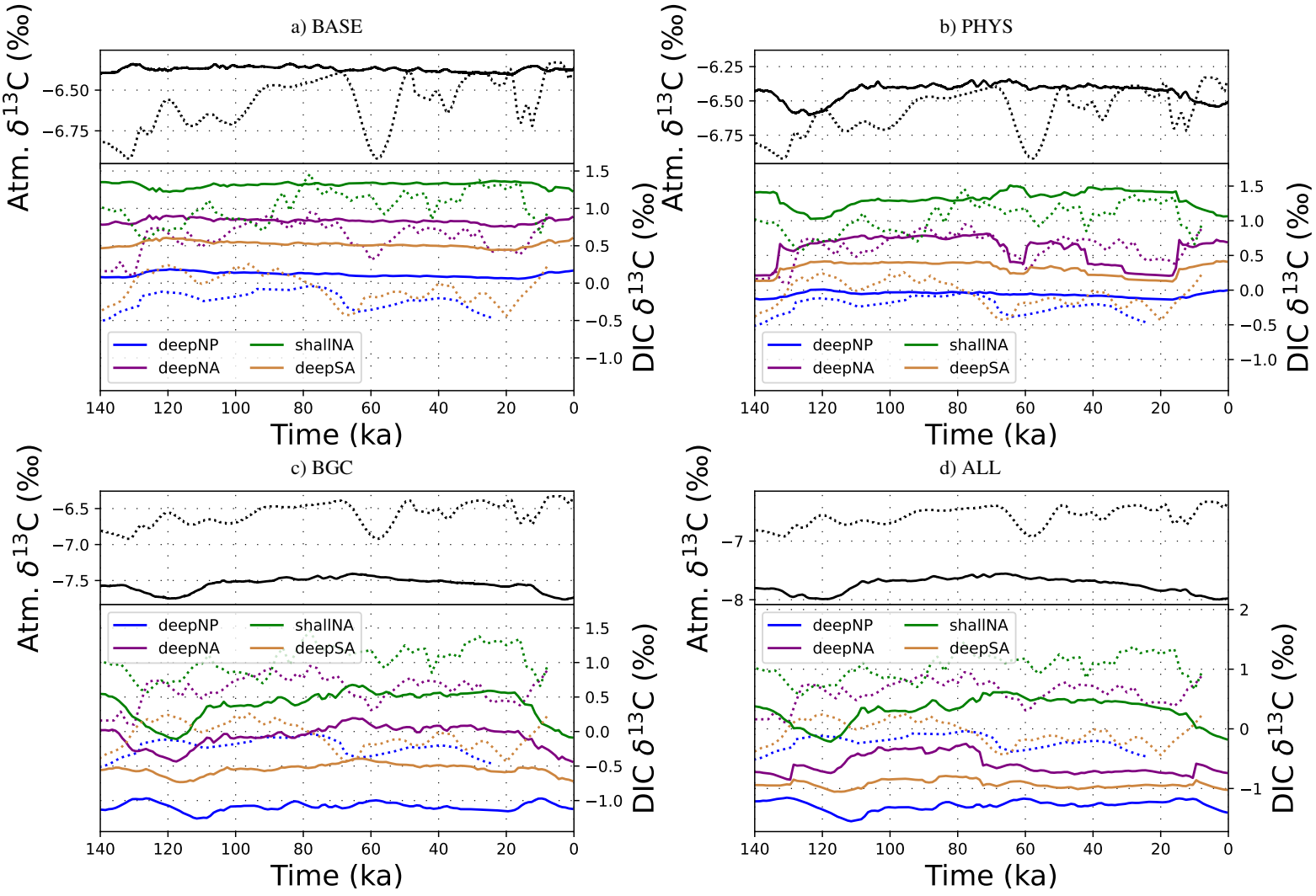

Figure S32. δ^{13}C over the most recent glacial cycle in various reservoirs. Full lines are simulations BASE, PHYS, BGC, and ALLC. Dotted lines are reconstructions from Köhler et al., 2010, Eggleston et al., 2016 and Barth et al., 2020.

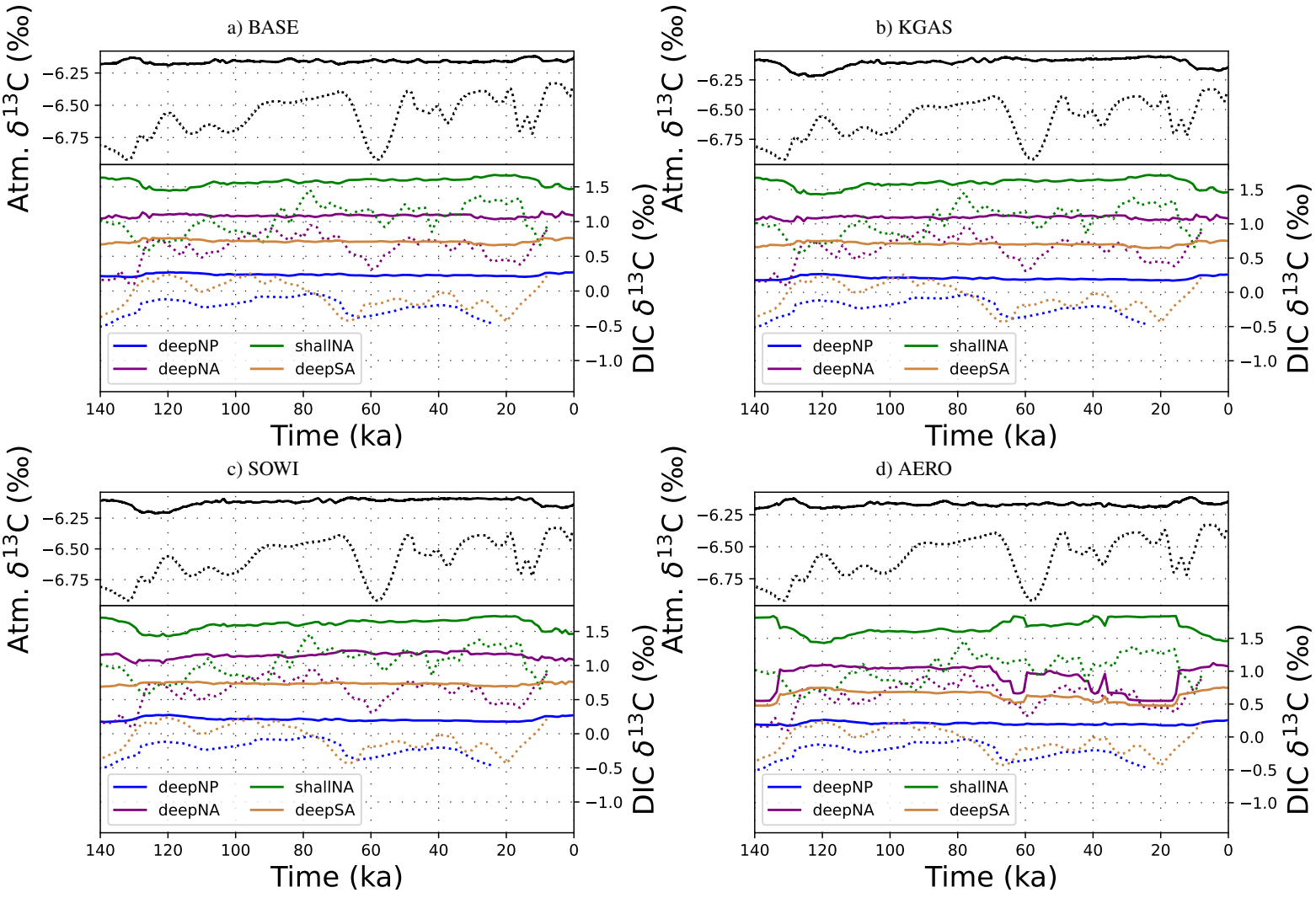

Figure S33. δ^{13}C over the most recent glacial cycle in various reservoirs. Full lines are simulation results with different physical forcings in a closed system, dotted lines are reconstructions from Köhler et al., 2010, Eggleston et al., 2016 and Barth et al., 2020

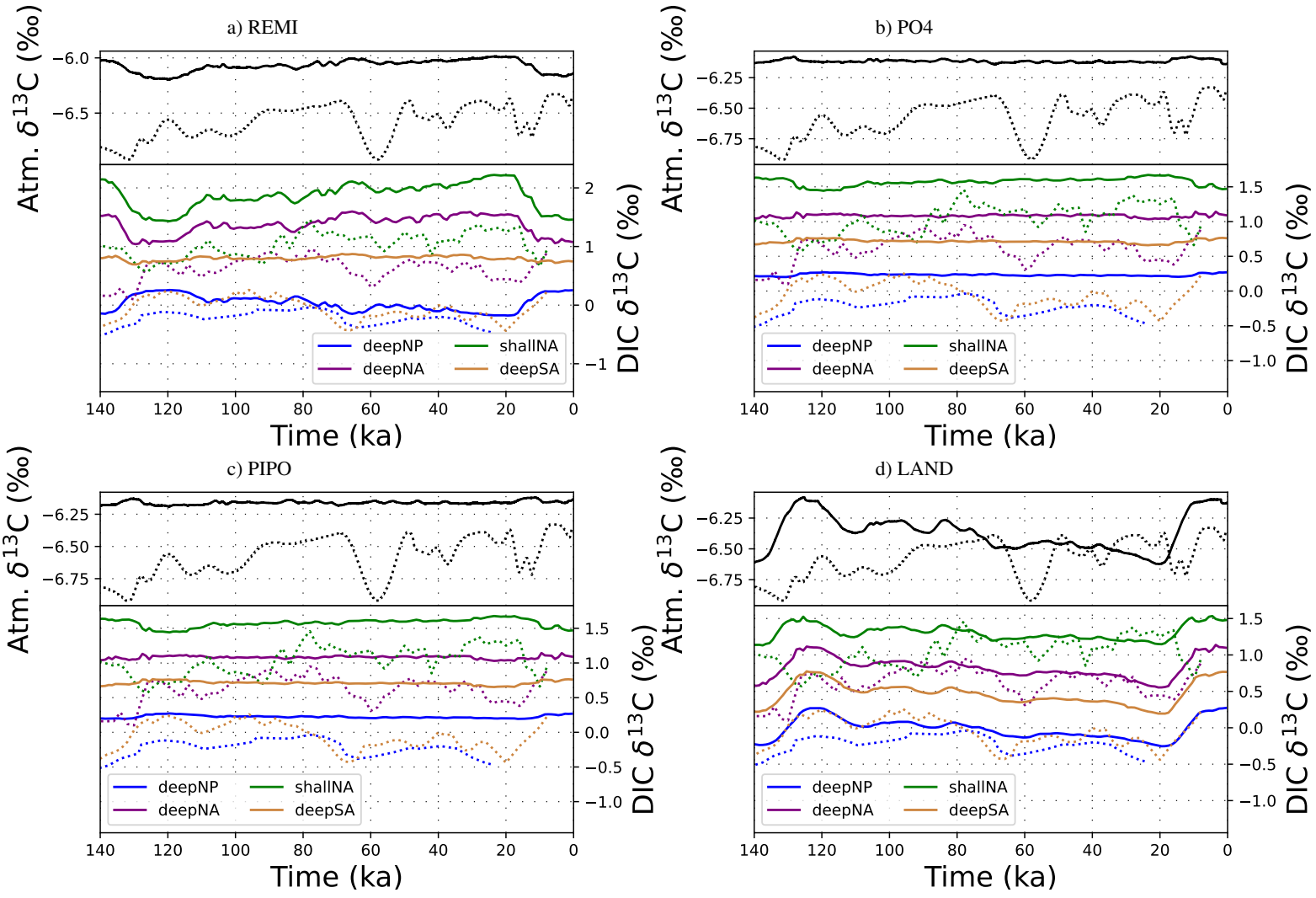

Figure S34. δ^{13}C over the most recent glacial cycle in various reservoirs. Full lines are simulation results with different biochemical forcings in a closed system, dotted lines are reconstructions from Köhler et al., 2010, Eggleston et al., 2016 and Barth et al., 2020

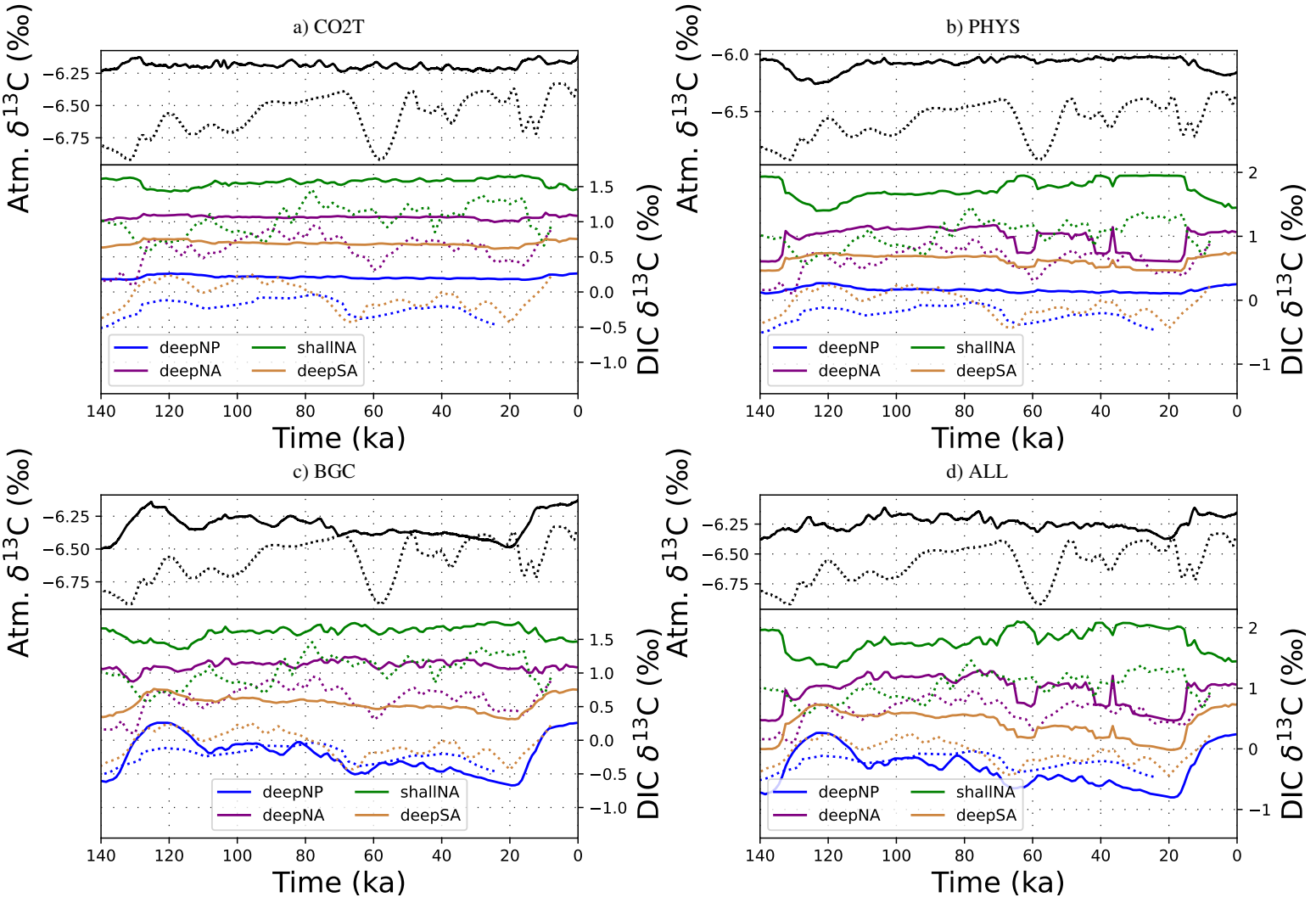

Figure S35. δ^{13}C over the most recent glacial cycle in various reservoirs. Full lines are simulations CO2T, PHYS, BGC, and ALLC in a closed system. Dotted lines are reconstructions from Köhler et al., 2010, Eggleston et al., 2016 and Barth et al., 2020.

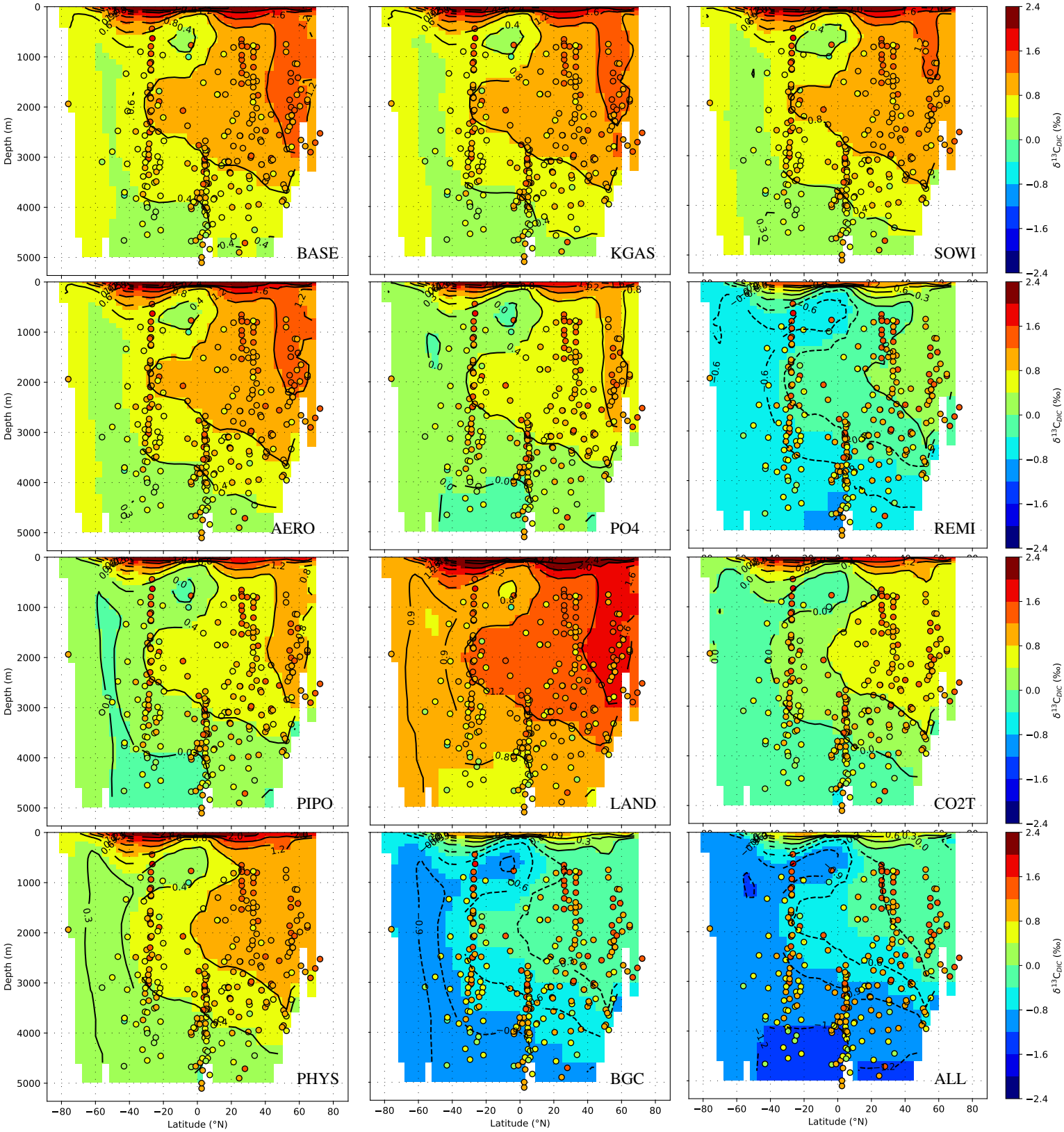

Figure S36. Simulated (open system) and reconstructed (compilation from Pöppelmeier et al. (2023)) Holocene δ^{13}C distribution Atlantic.

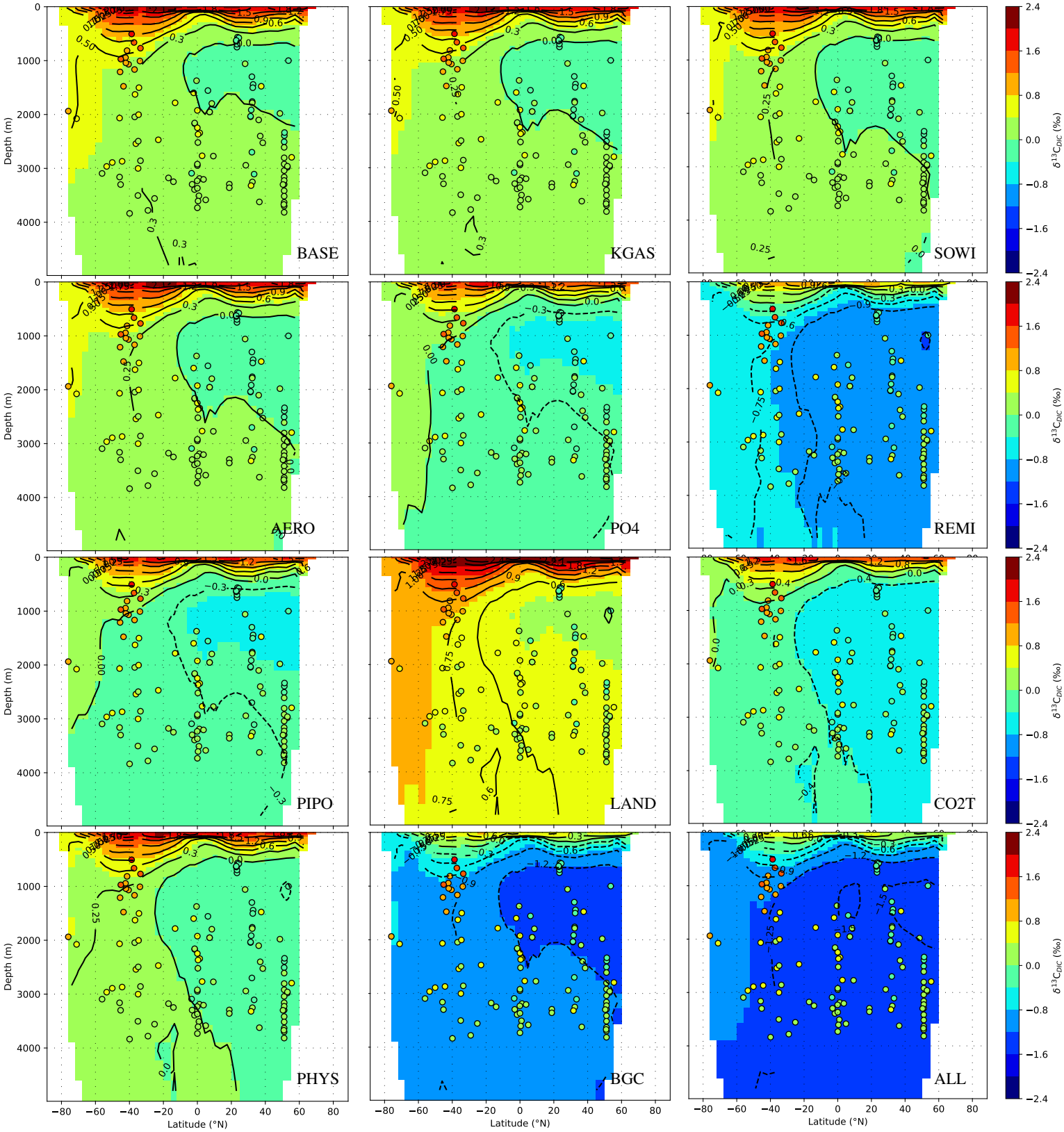

Figure S37. Simulated (open system) and reconstructed (compilation from Pöppelmeier et al. (2023)) Holocene δ^{13}C distribution Pacific.

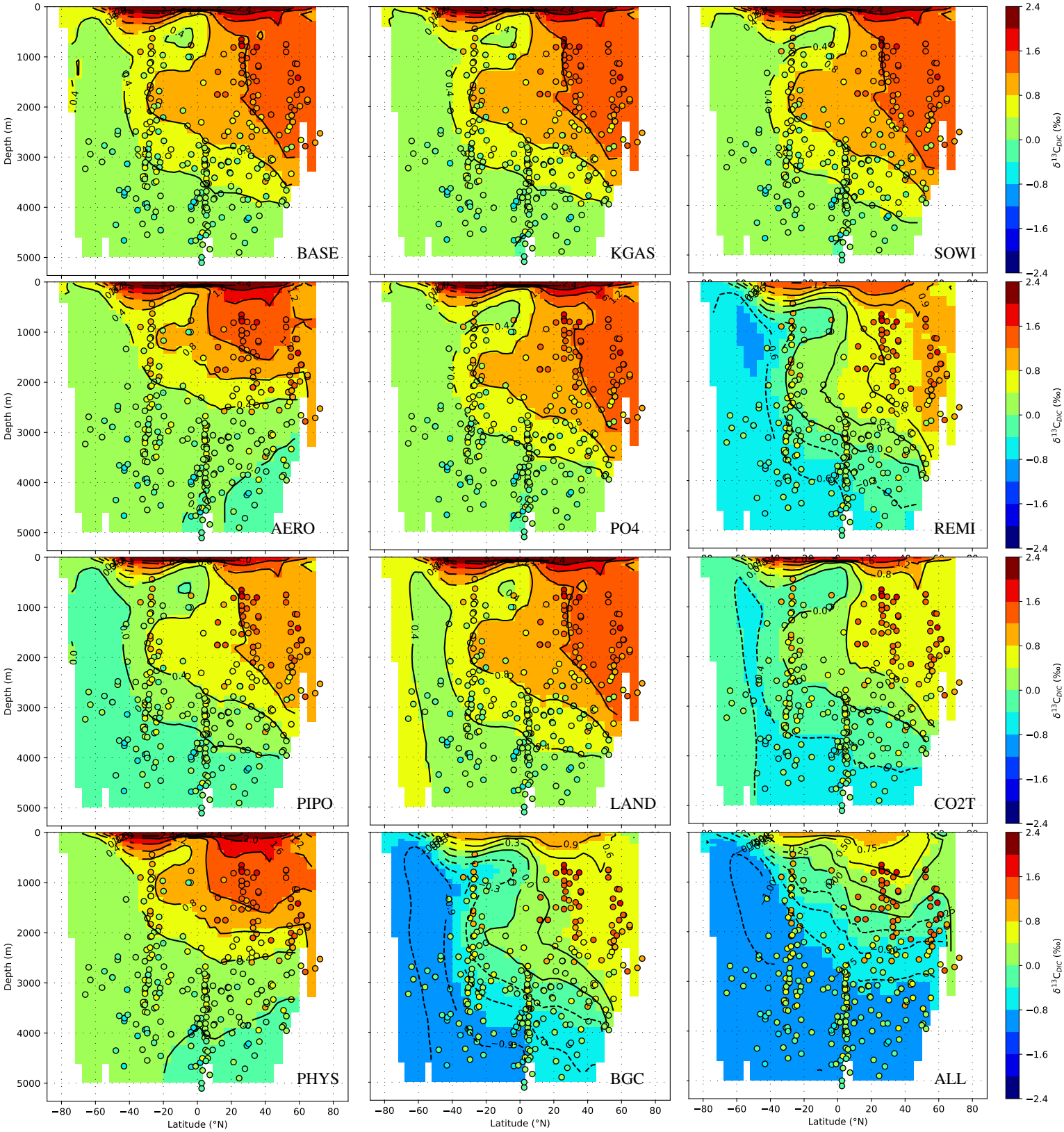

Figure S38. Simulated (open system) and reconstructed (compilation from Pöppelmeier et al. (2023)) LGM δ^{13}C distribution Atlantic.

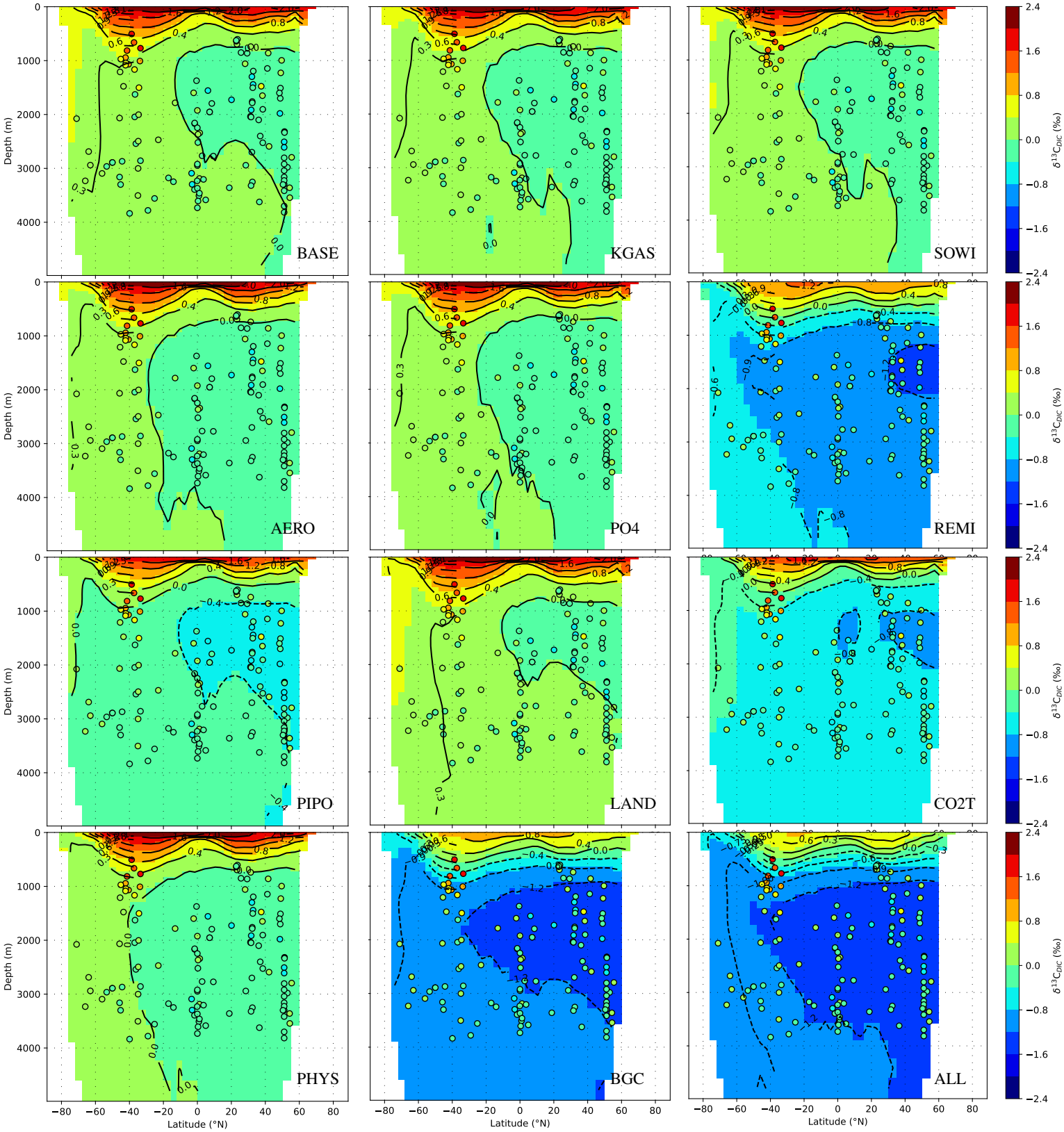

Figure S39. Simulated (open system) and reconstructed (compilation from Pöppelmeier et al. (2023)) LGM δ^{13}C distribution Pacific.

Table S1. Summary Model-Data comparison for simulations without interactive sediments

	$\Delta[CO_2]$ (ppm)	ΔpH	ΔPOM_{export} (g/m^2/yr)			$\Delta[PO_{4,pre}]$ (mmol/m^3)	$\Delta\delta^{13}C$ (‰)			$\Delta[CO_3^{2-}]$ (μmol/kg)
loc.	global	Eq. Atl.	Iber. Marg.	Eq. Atl.	polar SO	global	shall. NA	deep NA	deep Pac.	deep Pac.
time	PI - 18 ka	22 - 3 ka	22 ka - PI			21 ka - PI	20 - 8 ka		22 ka - PI	22 - 7 ka
Data	↑	↑	↑	↑	↓	↓	↑	↓	↓	↓
Factorial Results										
$fBASE$	↑	↑	↑	↑	↓	↑	↑	o	↓	↓
$fKGAS$	↑	o	o	↓	o	o	o	o	o	↑
$fSOWI$	↑	↑	↓	↓	↓	↓	↑	o	o	↑
$fAERO$	↑	↑	↓	↓	↑	↑	↑	o	o	↑
$fREMI$	↑	↑	↓	↓	o	↓	↑	o	↓	↓
$fPIPO$	↑	↑	↑	↑	o	o	o	o	o	↓
$fLAND$	↓	↓	o	o	o	o	↓	o	↓	↓
$fCO2T$	↑	↑	↑	o	↑	o	o	o	o	↑
$fPHYS$	↑	o	↑	↓	↑	↑	o	o	o	↑
$fBGC$	↑	o	↑	↑	o	o	o	o	o	↓
$nlADD$	↑	↑	↓	↑	o	o	o	o	o	↑
$nlTOT$	↑	↑	↓	↑	↑	↑	o	o	o	↓